PREPRINT
Phanerozoic thermochronology record of Afro-Arabia through space and time

Samuel C. Boone[1,2,3], Malcolm McMillan[2], Maria-Laura Balestrieri[4], Barry Kohn[2], Andrew Gleadow[2], Abaz Alimanovic[2], Graham Hutchinson[2], Wayne Noble[5], Vhairi Mackintosh[2], Christian Seiler[2,6], Dave Belton[2], Danielle Majer-Kielbaska[2], Daniel F. Stockli[7], Joachim Jacobs[8], Edgardo J. Pujols[7], Matthias Daßinnes[9], Benjamin Emmel[10], Fabian Kohlmann[5], and Romain Beucher[11]

Affiliations

1. University of Sydney, School of Geosciences, Camperdown, NSW 2050, Australia
2. University of Melbourne, School of Geography, Earth and Atmospheric Sciences, Parkville, VIC 3010, Australia
3. University of Adelaide, Department of Earth Sciences, The University of Adelaide, Adelaide, SA, 5005, Australia
4. Istituto di Geoscienze e Georisorse, Consiglio Nazionale delle Ricerche, UOS Firenze, Firenze, Italy
5. Lithodat Pty Ltd, Melbourne, Victoria 3030, Australia
6. Anglo American, 201 Charlotte Street, Brisbane QLD 4000, Australia
7. Department of Earth and Planetary Sciences, The University of Texas, Austin, Texas 78712, USA
8. University of Bergen, Department of Earth Science, P.O. Box 7803, N-5020 Bergen, Norway
9. Equinor ASA, EPN, 7502 Stjørdal, Norway
10. SINTEF Industry, 7465 Trondheim, Norway
11. Australian Earth-System Simulator National Research Infrastructure (ACCESS-NRI), Canberra, ACT 2601, Australia

corresponding author: Samuel C Boone (samuel.boone@sydney.edu.au)

Here we present a non-peer reviewed preprint submitted to EarthArXiv of the manuscript entitled, *Phanerozoic thermochronology record of Afro-Arabia through space and time*. This manuscript has been submitted to Scientific Data as a Data Descriptor Article for peer review and is currently under consideration.

The thermochronology database of eastern Africa and Arabia which this paper concerns is freely accessible via the AusGeochem data platform (soon to be renamed to EarthBank in the coming months), which enables users to geospatially interrogate the data in 4D (3D through time): https://doi.org/10.58024/AGUM97FC4439

Phanerozoic thermochronology record of Afro-Arabia through space and time

Samuel C. Boone[1,2,3], Malcolm McMillan[2], Maria-Laura Balestrieri[4], Barry Kohn[2], Andrew Gleadow[2], Abaz Alimanovic[2], Graham Hutchinson[2], Wayne Noble[5], Vhairi Mackintosh[2], Christian Seiler[2,6], Dave Belton[2], Danielle Majer-Kielbaska[2], Daniel F. Stockli[7], Joachim Jacobs[8], Edgardo J. Pujols[7], Matthias Daßinnes[9], Benjamin Emmel[10], Fabian Kohlmann[5], and Romain Beucher[11]

Affiliations

1. University of Sydney, School of Geosciences, Camperdown, NSW 2050, Australia
2. University of Melbourne, School of Geography, Earth and Atmospheric Sciences, Parkville, VIC 3010, Australia
3. University of Adelaide, Department of Earth Sciences, The University of Adelaide, Adelaide, SA, 5005, Australia
4. Istituto di Geoscienze e Georisorse, Consiglio Nazionale delle Ricerche, UOS Firenze, Firenze, Italy
5. Lithodat Pty Ltd, Melbourne, Victoria 3030, Australia
6. Anglo American, 201 Charlotte Street, Brisbane QLD 4000, Australia
7. Department of Earth and Planetary Sciences, The University of Texas, Austin, Texas 78712, USA
8. University of Bergen, Department of Earth Science, P.O. Box 7803, N-5020 Bergen, Norway
9. Equinor ASA, EPN, 7502 Stjørdal, Norway
10. SINTEF Industry, 7465 Trondheim, Norway
11. Australian Earth-System Simulator National Research Infrastructure (ACCESS-NRI), Canberra, ACT 2601, Australia

corresponding author: Samuel C Boone (samuel.boone@sydney.edu.au)

Abstract

Low-temperature thermochronology has been widely used in eastern Africa and Arabia (Afro-Arabia) to investigate the long-term thermal evolution of the crust in response to Phanerozoic tectonism. Yet, utilisation of this invaluable thermochronology record to inform numerical investigations into the long-term tectonothermal, geodynamic and landscape evolution of the region has been limited by the dispersion of these data across numerous disparate case studies. Here, we present a relational database of apatite (1787), zircon (68) and titanite fission-track (97) analyses, and apatite (1,945), zircon (3310), and titanite (U-Th)/He (83) ages, including 465 new fission-track and 2,583 new single-grain (U-Th)/He analyses from across region. Where available, all detailed single-grain age, track length, geochemical and kinetic parameter data needed for performing thermal history modelling are presented. Also included are 668 digitised thermochronology-derived thermal history simulations and burial history models from well data, which quantify the regional upper crustal Phanerozoic thermal history. Collectively, this comprehensive database records the Phanerozoic thermal evolution of Afro-Arabia through space and time. Regional spatiotemporal trends, anomalies, limitations and potential future uses of the dataset are then discussed.

The machine-readable database is made publicly available through the EarthBank platform, enabling 4D (3D through time) geospatial data interrogation.

Background & Summary

Occupying the core of Gondwana since its formation in the late Neoproterozoic, eastern Africa and Arabia have experienced multiple periods of superimposed Phanerozoic extensional tectonism and related magmatism, periodically interrupted by spatiotemporally restricted compressional events, as the great southern hemisphere megacontinent slowly but inexorably broke apart (Fig. 1). Beginning with widespread extension throughout southern and eastern Africa during regional Permo-Triassic Karoo rifting[1], the central Gondwanan lithosphere eventually began to rupture in the Jurassic as first Antarctica and then a still coupled Madagascar-India broke away from Africa and migrated to the south and east, respectively[2]. Widespread normal faulting, basin formation and subsidence continued through the Cretaceous and into the Paleogene along the passive East African margin and across much of northern Africa[3,4].

This prolonged period of megacontinental disintegration eventually culminated in the development of the Eocene-recent Afro-Arabian Rift System (AARS), with extensional strain primarily accommodated along the three-pronged Red Sea, Gulf of Aden and East African Rift System (EARS). Nucleating first in the late Paleogene in discrete zones of extensional strain and magmatism in the Turkana Depression[5–8], Afar[9,10], and Rukwa rift sectors[11] above a mantle superplume impinged beneath eastern Afro-Arabia[7], the AARS has gradually propagated outwards to form a near continuously linked system of rift basins by the Quaternary[12]. As a result, the Nubian (African), Somalian (East African) and Arabian plates, along with the Victorian and Rovuma microplates of central Africa, have been kinematically decoupled[13]. This has enabled Arabia to independently migrate northeastwards since the Miocene leaving the newly formed oceanic lithosphere beneath the Gulf of Aden and Red Sea in its wake[14,15]. Meanwhile, the Somalian plate has rotated clockwise relative to Nubia as the East African Rift continues to accommodate ~E-W extension and normal faulting propagates southwards into the nascent rifts of the Okavango and Mozambique Channel[13,16].

Pinpointing the spatiotemporal chronology of these tectonic events through deep time and thus the geodynamic systems governing these processes has, however, proved challenging. This is in part because the geological strata which directly record these phenomena in the deep past are often poorly preserved in outcrop, and publicly accessible subsurface data remain sparse. While geophysical techniques have provided a powerful toolset with which to assess the thermomechanical state of the Afro-Arabian lithosphere and underlying asthenosphere[17–19], the snapshots which these data afford are restricted to the present-day and must be ‘reconstructed’ back through time to develop models of asthenospheric convection and lithospheric deformation processes operating in the deep past. These geodynamic simulations are themselves often very difficult to validate. Other geoscientists have turned to geochemistry as a tool for constraining the timing and rate of geological processes directly recorded in the chemical and isotopic composition of geological materials. This has included high-temperature geochronology, isotope geochemistry and major, minor and trace element geochemistry, which have been particularly important for tracking the magmatic history of the region[8,20–22] and the metamorphic evolution of the Afro-Arabian crust[23–25].

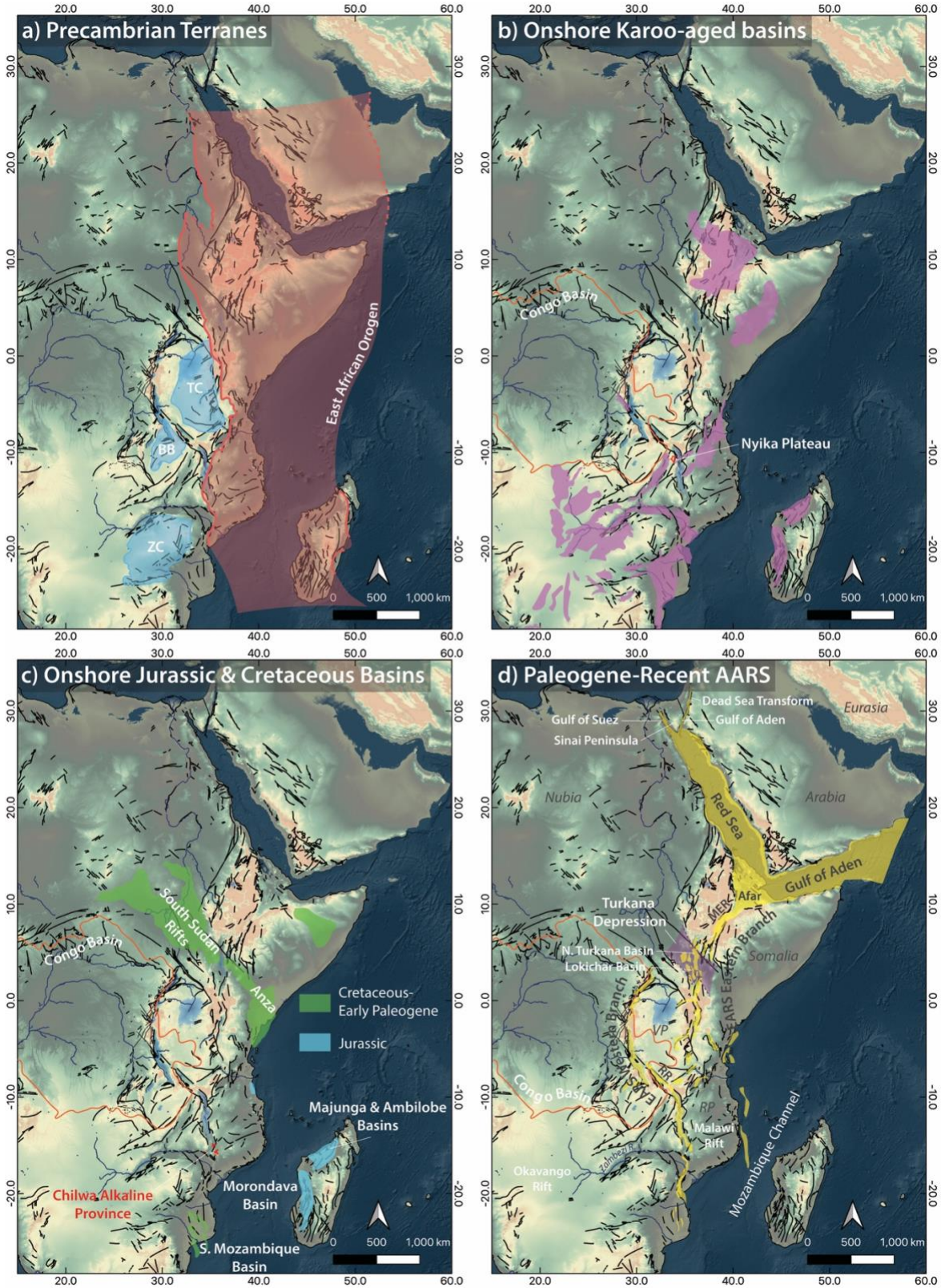

Figure 1. Key geological terranes and features of eastern Africa and Arabia discussed in the text. Distribution of cratons, orogenic belts and basins after Purcell[26], Davison and Steel[3], and Collins et al.[24]. Fault map is from Thiéblemont et al.[27].

However, to constrain past lower-temperature geological processes which operated in the middle to upper crust, geoscientists have instead had to rely on so-called low-temperature thermochronology techniques. Applied primarily to outcropping Precambrian crystalline granitoids and metamorphic assemblages, and to a lesser degree Phanerozoic sedimentary rocks sampled at the surface or at depth in boreholes, these temperature-sensitive dating techniques have enabled geoscientists to directly constrain the thermal evolution of the Afro-Arabian upper crust in response to multiple, superimposed periods of orogenesis, rifting, magmatism, hydrothermal fluid flow, dynamic uplift, and long-term erosion. In particular, apatite fission track (AFT) and (U-Th)/He (AHe) analyses have been widely utilised in an effort to constrain the timing and rate of rift-related, upper crustal thermal perturbations between ~30 and 120 °C (up to ~5 km depth)[5,28,37–46,29,47–56,30,57–66,31,67–76,32,77–86,33,87–91,34–36]. In turn, these provide insights into the spatio-temporal evolution of individual rift basins[5,28,41,42,66,71,79,92,93], development of rift-related topography[67,78,83], normal fault system growth[62,68,94], sediment provenance[89,95], and, in some cases, the thermal influence of igneous intrusions and circulation of heated fluids[86]. In many cases, these data have been complemented by the utilisation of higher temperature thermochronometers, such as zircon and titanite fission track (ZFT and TFT, respectively) and (U-Th)/He (ZHe and THe, respectively) to investigate periods of mid-crustal exhumation related to older tectonic events which shaped the lithospheric architecture in which the AARS developed[35,36,65,67,73,78,82,84,86,96,97,40–42,44,45,56,63,64], date igneous intrusions[53,75], or as a tool for tracking source-to-sink sediment transport histories[89,95].

However, the relatively limited number of samples and confined spatial extent of individual case studies have precluded insights into longer wavelength tectonic and geodynamic phenomena, such as regional denudation trends and the growth of topography due to plume impingement. This has spurred authors to begin synthesising low-temperature thermochronology data on regional scales in an effort to constrain the spatio-temporal evolution of entire rift segments, such as in the wider Red Sea and Gulf of Aden[92,98,99]. Yet, the raw data which underpin these regional syntheses remain buried in the many dozens of publications and associated appendices, requiring readers to manually mine these data if they wish to make use of them in their research.

Here, we present a synthesis of 1787 AFT, 68 ZFT, 97 TFT, 1,715 single grain and 230 multi-grain aliquot AHe, 3310 single-grain ZHe, and 61 single-grain and 22 multi-grain aliquot THe ages from across the greater Afro-Arabian Rift System region, representing every known low-temperature thermochronology analyses to exist from the area as of March 2023 (Fig. 2). This comprehensive dataset includes 465 new fission-track and 2,583 new single-grain (U-Th)/He analyses from 833 rock samples from Egypt, Ethiopia, Kenya, Malawi, Mozambique, and Zimbabwe which are previously unpublished. Where available, we also present the associated electron probe microanalysis (EPMA) data that was collected in tandem with AFT analysis. The database also includes an additional 668 digitised thermochronology-derived thermal history models and burial history models from well data (Fig. 3), which quantify the Phanerozoic time-temperature paths of outcrop and near-surface rocks in these locations.

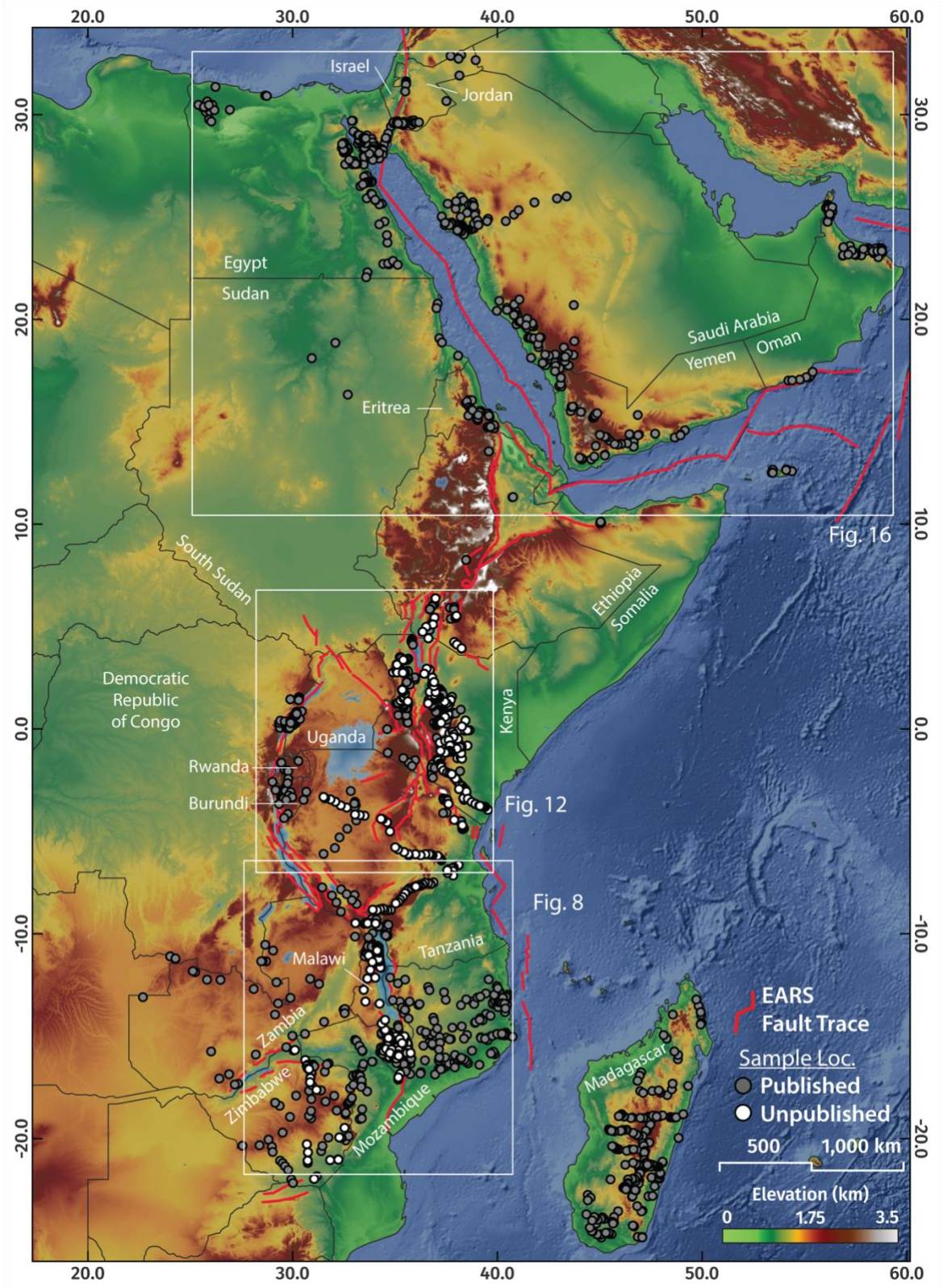

Figure 2. The greater Afro-Arabian Rift System region showing previously published and previously unpublished low-temperature thermochronology localities.

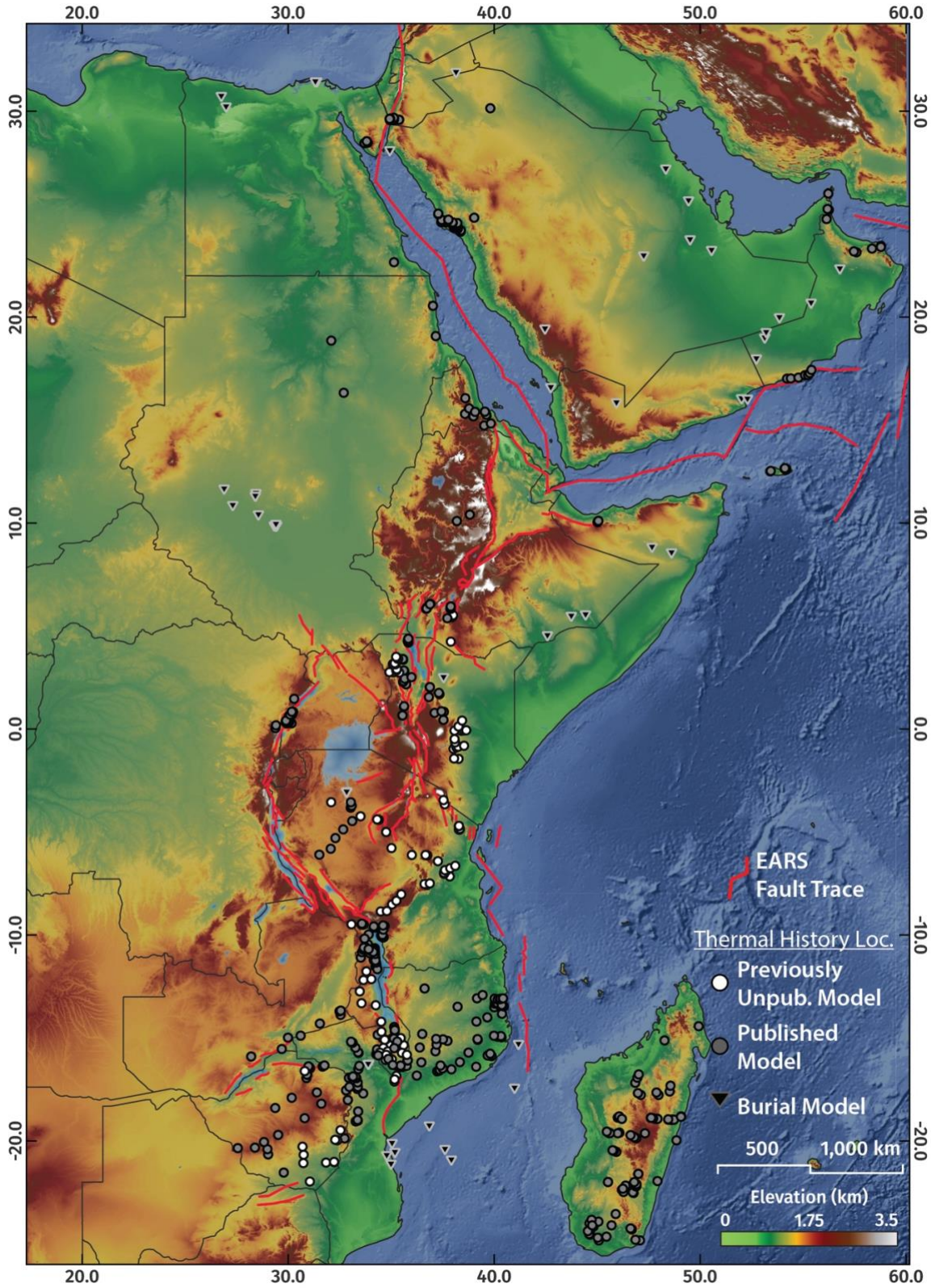

Figure 3. The greater Afro-Arabian Rift System region showing the locations of digitised published and previously unpublished thermal history simulations and burial history models.

The entire database is made publicly available via EarthBank (formerly called AusGeochem)[100,101], an open-access geospatial data platform which enables geochemical, geochronological and thermochronological analyses to be disseminated and interrogated in 4D (3D through time). In addition to the sheer number of analyses, the level of data granularity is also unprecedented in low-temperature thermochronology databases, with all available measured parameters and analytical metadata included to maximise the utility of this powerful dataset.

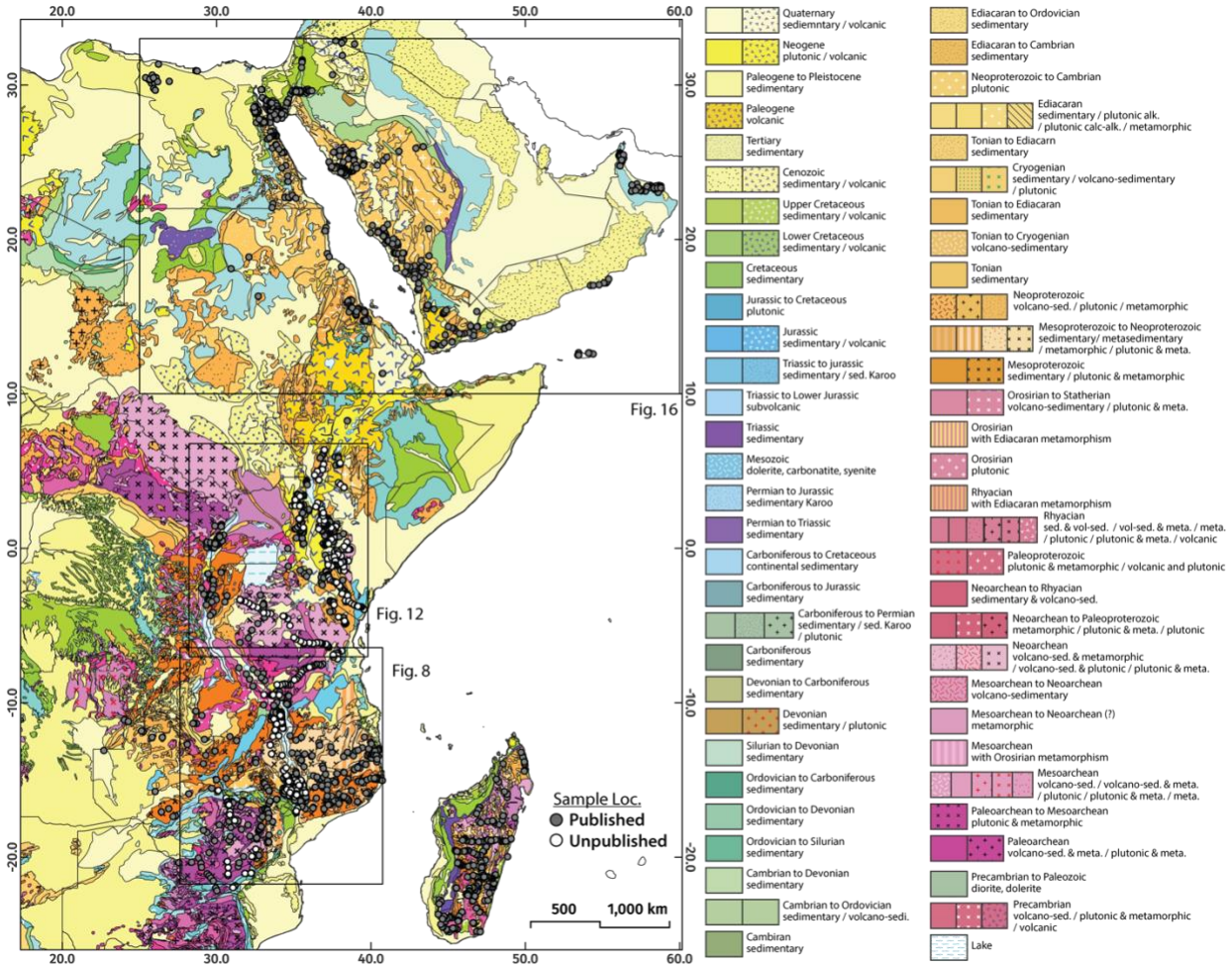

Figure 4. Simplified geological map of the greater AARS region showing the spatial distribution of thermochronology samples. Geological base map sourced from Thiéblemont et al.[27].

This continental-scale low-temperature thermochronology synthesis provides novel insights into the upper crustal evolution of the AARS that were previously difficult to decipher from an otherwise cumbersome and intractably large dataset. The data record a series of pronounced episodes of upper crustal cooling related to the development of the Red Sea, Gulf of Aden, and East African Rift System (EARS) since the late Paleogene. In addition, they provide insights into the inherited Phanerozoic tectono-thermal histories of these regions which controlled the spatial and temporal distribution of subsequent igneous activity and extensional strain. Taken together, this dataset provides an invaluable geochemical record of the

Phanerozoic thermal evolution of East Africa and Arabia with which to validate future tectonic studies and numerical geodynamic and landscape evolution models of the region.

Below, we describe the distribution and limitations of sampled localities and lithologies, and the employed methodologies for legacy data collation and new data acquisition. Regional patterns in thermochronology data are then discussed, highlighting anomalies and peculiarities in intra- and intersample data trends that may warrant further future investigation.

Methods

Thermochronometers, such fission track and (U-Th)/He analysis, are temperature sensitive radiometric dating techniques where the retention of radiogenic daughter products in a mineral sample is a product of time, temperature, cooling rate and crystal chemistry[102,103]. To quantify the thermal histories which these data record, numerical thermal history modelling is often performed using programs such as QTQt[104] and HeFTy[105] and published fission-track annealing[106] and He diffusion models[107–110]. The time-temperature histories of geological materials recorded by thermochronology can thus provide important constraints for the advection of mass and heat in the crust, which generally reflect processes such as tectonic exhumation, erosional denudation and subsidence, or in some instances, conductive heating due to changes in crustal heat flow, magmatism or hydrothermal activity[111–113].

The titanite, zircon and apatite fission-track and (U-Th)/He database presented herein consists of a compilation of 4,227 published and 3,048 new, previously unpublished low-temperature thermochronology data from the greater Afro-Arabian Rift System region. For previously published work, detailed geosample and analytical (meta)data were mined from their respective publications, cleaned and compiled into the relational thermochronology data models of Boone et al.[101], to enable more efficient reutilisation of these invaluable data by the scientific community. For descriptions of the methodologies employed to generate these data, readers should refer to their associated references, all of which are listed along with the data in the datafiles. The analytical methodologies for the newly published data are presented below.

The compilation also includes 668 digitised thermal history models, comprised of 70 published burial history models generated from well data[73,114,123–132,115,133–137,116–122] and 598 thermochronology-derived thermal history models (111 previously unpublished), the metadata and resulting simulated time-temperature paths of which are included in this database.

Thermochronology Samples

The thermochronology data presented in this compilation were acquired from 2449 rock samples (primarily Precambrian metamorphic and igneous lithologies), 85.9% of which were collected from surface outcrops from elevations ranging from 0 to 4144 m above sea level (Figs. 4 & 5). The remaining 14.1% were collected from boreholes and exploration wells down to depths of 936 m below the surface.

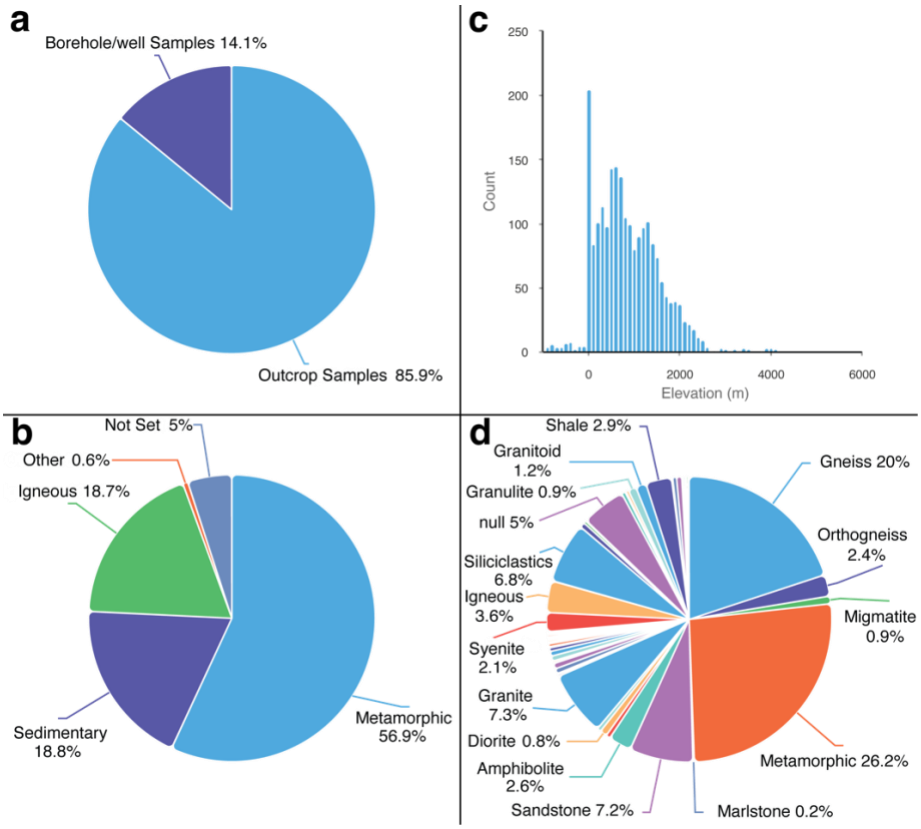

Figure 5. Geological sample metadata. Histogram and pie charts generated with EarthBank[100] show the breakdown of sample types (a), elevations (b), rock types (c) and lithologies (d) in the database (n = 2449 geological samples).

Apatite Fission Track Thermochronology

Fission-track analysis is based on the spontaneous fission of naturally occurring ^{238}U and the resulting formation of crystallographic damage trails in a uranium-bearing mineral, called fission tracks[102,138,139]. Above a certain temperature specific to the mineral system in question, fission tracks anneal nearly instantaneously, while below some other lower temperature, nearly the full, original fission-track length is retained. However, between these temperatures in what is called the partial annealing zone (PAZ), fission tracks anneal progressively as a function of time, temperature, cooling rate and chemistry[106,140]. For the apatite fission-track (AFT) system, the PAZ is typically between ~60 and ~ 110–120 °C for fluorapatite, over geological timescales[141], depending on mineral composition and the duration of heating[142,143]. For the higher temperature sensitive titanite fission-track (TFT) and zircon fission-track (ZFT) methods, the PAZ corresponds to ~310–265 °C and ~ 350–200 °C, respectively[144–150]. By combining fission track age and the distribution of confined fission track lengths (often statistically represented by a mean track length (MTL) and standard deviation), the thermal history of a sample within the PAZ can be determined[104,105].

External Detector Method Fission Track Analysis

Previously unpublished external detector method (EDM) fission track analyses presented herein were performed across two laboratories: the Istituto di Geoscienze e Georisorse, Consiglio Nazionale delle

Ricerche, in Firenze, Italy and in the former home of the Melbourne Thermochronology Research Group at La Trobe University in Melbourne, Australia.

For all EDM analyses, apatite grains were mounted in epoxy resin, ground, and polished to expose internal mineral surfaces. Samples were etched with 5M HNO_3 at 20 °C for 20 s to reveal spontaneous fission tracks intersecting the polished internal apatite crystal surfaces. Samples were covered with a uranium-free muscovite external detector and irradiated with thermal neutrons; those analysed at the Istituto di Geoscienze e Georisorse were irradiated at the Laboratorio Energia Nucleare Applicata Triga Mark II reactor at Pavia University, Italy, while those analysed at La Trobe were irradiated at the Australian Institute of Nuclear Science and Technology Organisation HIFAR reactor. Induced fission tracks in the external detector were revealed by etching the mounts in 40% HF at room temperature for 40 min.

Fission track counting and length measurements of EDM samples from Ethiopia was performed by author Maria Laura Balestrieri on a Zeiss Axioskop (under a nominal dry objective magnification of 1250x) equipped with a Kinetek automatic stage at the CNR-IGG Fission-Track laboratory. The Trackkey 4.2 Program was used for all AFT age calculations procedures[151] using a ζ-calibration of 360 ± 11.

Determination of fission track densities and the measurement of horizontal-confined track lengths for all remaining EDM samples were performed at La Trobe University by authors Wayne Noble (ζ-calibration of 354 ± 7) and Dave Belton (ζ-calibration of 362.4 ± 12) using an Autoscan TM stage system and a HIPAD TM digitizing tablet, in conjunction with a Zeiss microscope (at 1250x magnification) with dry objectives and a drawing tube.

For all EDM analyses, a chi-square (χ^2) test was carried out on the AFT single-grain age in order to test homogeneity of data[152]. The probability of (χ^2) was calculated for each sample: if $P(\chi^2) > 5\%$ then the sample is assumed to be comprised of a single population of single-grain ages[153].

Track-pit opening diameters parallel to the crystallographic c-axis (Dpar) were measured for each grain as a proxy for the compositional control on fission track annealing kinetics[142]. Dpar lengths have been shown to correlate with various chemical compositions that affect annealing, such as Cl, F, and OH. In general, apatite grains with longer Dpars show increased resistance to annealing and are likely correlated with higher concentrations of Cl and OH with respect to F[154].

Laser Ablation Inductively Coupled Plasma Mass Spectrometry Fission Track Analysis

New laser ablation inductively coupled plasma mass spectrometry (LA-ICP-MS) fission track analyses were performed at the University of Melbourne Thermochronology Laboratories in Melbourne, Australia following the analytical protocol of Seiler et al.[155]. For each sample, two apatite grain mounts (FT counting and FT length) were prepared using two-part cold-set epoxy on glass slides. Both slides were polished to a 1 μm finish on a Struers Rotopol automated polishing machine using diamond pastes. Slides were then etched in 5M HNO3 at 20 °C for 20s. Analyses were performed on stacked image sets from the grain surface to a depth of ~15 μm in both reflected and transmitted light. Digital images were autonomously captured by TrackWorks using a 4.0 MP IDS uEye UI-3370CP-C-HQ camera mounted on a Zeiss M1m AxioImager microscope with a 1,000x total magnification and a 100x dry objective (calibration = 0.0873/0.0873 μm/pixel). On average, 30 suitable grains were selected for counting spontaneous fission track density

determinations. Track counting was conducted automatically by FastTracks using the "coincidence mapping" technique of Gleadow et al.[156] and manually corrected where necessary. Uranium concentrations of each grain were determined by LA-ICP-MS single spot analysis using a New Wave Nd:YAG Laser (λ = 213 nm with 5 Hz @ 56%–57% power, spot size = 30 μm, ~8 μm ablation depth) carried with Ar gas to an Agilent 7700 mass spectrometer. The well-characterized Durango apatite and an in-house sintered Mud Tank carbonatite apatite were used as secondary reference materials for LA-ICP-MS data quality assessment. Single grain and pooled ages were calculated according to Seiler et al.[155] using an ξ-calibration of $2.185 \pm 0.134 \times 10^{-3}$. Central ages were calculated following Vermeesch[157], recasting 0-track grains to an EDM-like form.

Confined track lengths (Track-In-Track [TINT] only) were measured as true-dip corrected 3D lengths up to 20° using FastTracks after irradiation by ^{252}Cf (to increase TINT occurrence) and corrected for a 1.634 refractive index (apatite).

Electron Probe Microanalysis

It has been shown that many compositional factors may influence thermal annealing of fission tracks in apatite, specifically cation substitutes[143,158], implying that Dpar has significant limitations as a standalone parameter. Thus, in addition to measuring Dpars as a proxy for grain composition, chemical compositions of individual apatite crystals for all LA-ICP-MS fission track analyses were directly measured on a per-grain basis via electron probe microanalysis (EPMA). A JEOL JXA-8530F FEG electron probe microanalyser was used with 5 WDS channels and an SDD EDS detector operating at an accelerating voltage of 15 kV and beam current of 10 nA with a 10 μm beam diameter. For all new LA-ICP-MS fission track analyses, this included measurements of F, P, Cl and Ca. For the most recently obtained LA-ICP-MS fission track results from samples from the Malawi rift sector, additional EPMA measurements of Sr, Na, Ce, La, Mn, Mg, Fe, K, Y, S, and Si were also obtained. For these, the multi-compositional model of Ketcham et al.[106] was employed to compare the annealing resistance of individual grains via a proxy (rmr0, Eq. 11; Ketcham et al.[106]).

Zircon and Apatite (U-Th)/He Thermochronology

(U-Th)/He thermochronology is based on the production of ^{4}He during the radioactive decay of ^{238}U, ^{235}U, ^{232}Th and, to a lesser degree, ^{147}Sm. However, the ^{4}He contribution from the decay of ^{147}Sm generally constitutes <1% of total radiogenic ^{4}He and is therefore often considered statistically insignificant when analysing U and Th-rich minerals, such as zircon. However, in some U- and Th-poor minerals, such as apatite, the consideration of the radioactive decay of ^{147}Sm is required. ^{4}He diffusivity is principally a function of time, temperature, crystal size, and accumulated radiation damage[108,159–161], though a range of additional crystallographic and compositional factors can result in overly dispersed ages (see discussions in Wildman et al.[162] and Danišík et al.[163]). In apatite, ^{4}He diffusion accelerates significantly above ~40 °C and nearly instantaneously above ~80 °C[164]. Between these temperatures in what is called the apatite (U-Th-Sm)/He (AHe) partial retention zone (PRZ), ^{4}He is partially retained. The zircon (U-Th)/He (ZHe) system is sensitive to higher temperatures, with the zircon partial retention zone (ZHe PRZ) typically ranging between ~130 and 200 °C[165–167], though this can be significantly lower in grains with high amounts of accumulated radiation damage[108]. The PRZ of the titanite (U-Th)/He (THe) system ranges between ~180–100 °C[168].

Previously unpublished apatite and zircon (U-Th)/He analyses presented here were obtained in the University of Melbourne Thermochronology Laboratories. The analytical procedure outlined in Gleadow et al.[169] were employed (except that for ZHe analysis, ^{233}U and ^{229}Th spikes were used), with Durango apatites and Fish Canyon Tuff zircons being used as internal standards.

Clear, euhedral, non-fractured apatites and zircons were separated manually by hand picking under an Olympus SZX12 binocular microscope and measured in order to apply the α-ejection correction of Farley et al.[170]. Grains were then placed in ethanol and checked for inclusions under polarized light. Apatites, placed in acid-treated platinum capsules, were outgassed under vacuum at ~900 °C for 5 min, using a semiconductor Coherent Quattro FAP 820-nm diode laser with fiber-optic coupling to the sample chamber. Zircons were outgassed using a laser power of ~12.6W (~1300°C) applied for 20 min to ensure complete extraction of ^{4}He. A hot blank was run after each gas extraction to verify complete outgassing of the apatite grains. The second re-extract contributed less than 0.5% of the total measured ^{4}He for all samples. ^{4}He content was measured by isotope dilution using a pure ^{3}He spike, measured using a Balzers Prisma QMS 200 quadrupole mass spectrometer and calibrated against an independent ^{4}He standard.

Once outgassed, grains were removed from the laser chamber, dissolved and analysed for parent isotopes using an Agilent 7700X ICP Mass Spectrometer. The degassed apatites were then dissolved in their capsules using HNO_3 for analysis of ^{238}U, ^{235}U, ^{232}Th and ^{147}Sm. AHe analyses were calibrated using the reference material BHVO-1, with Mud Tank Carbonatite apatite, and international rock standard BCR-2 used as check standards with each batch of samples analysed. AHe ages were calculated and corrected for α-emission following the approach of Farley et al. (1996).

Zircon grains were removed from their Pt capsules, transferred to Parr bombs, spiked with ^{235}U and ^{230}Th and digested in small volumes (0.3–0.5 ml) at 240 °C for 40 hours in HF. Standard solutions containing the same spike amounts as samples and unspiked reagent blanks were treated identically. A second bombing in HCl for 24 h at 200 °C ensured dissolution of fluoride salts. Zircon solutions were then dried down, dissolved in HNO_3 and diluted in H_2O to 5% acidity for analysis of ^{238}U, ^{235}U, and ^{232}Th by solution ICP-MS.

Analytical uncertainties, including the α-ejection correction, an estimated 5-μm uncertainty in grain dimension, gas analysis (<1%), and ICP-MS analytical uncertainties, are conservatively assessed at ~6.2%. Accuracy and precision of U, Th, and Sm content range up to 2% but are typically <1%.

Thermal History and Burial History Models

Numerical thermal history models provide invaluable information about temporal, as well as spatial trends in upper crustal thermal histories. Only by time stamping periods of crustal thermal flux recorded by these data can the rates of geological thermal processes be determined and their potential temporal correspondence to other geodynamic and tectonic events be established. This also enables the use of these data as parameters or validation datasets for numerical geodynamic and landscape evolution models, which can simulate the thermal or exhumation history of the crust over geological timescales.

Thus, published thermal history models were also digitised where available, and archived in the relational data model format of Boone et al.[101]. Using the open-access WebPlotDigitizer software (version 4.2), best-fit, upper and lower 95% confidence envelope thermal history paths were extracted from published time-temperature plots. In addition, metadata pertaining to the modelling parameters and simulation goodness of fit were collated, enabling independent model quality assessment.

For a 111 of the newly analysed samples, such as for previously unpublished thermochronology data from northwest Kenya, new thermal history modelling was performed to quantify the thermal evolutions which these data record. For previously unpublished data in Kenya, Ethiopia, Malawi and Zimbabwe, joint inverse numerical thermal history modelling of ZHe, AHe and AFT data was performed using QTQt[104], using the multi-compositional AFT annealing model of Ketcham et al.[106], the ZHe radiation damage accumulation and annealing model of Guenthner et al.[108], and the AHe diffusion model of Gautheron et al.[109]. Only 1- and 2-termination ZHe and AHe grains were modelled, due to the tendency of 0-termination grains to yield significantly larger age dispersion[171]. A present-day surface temperature constraint of 20 ± 10°C was applied to all models. The time-temperature modelling space was set as the oldest thermochronology age ± the oldest thermochronology age for that sample, along with the temperature range of 100 ± 100°C. Thermal history modelling was first performed using AFT data only, before adding ZHe and AHe data in subsequent model runs. In two instances (samples TUB13-74 and TUB15-07), inverse models that included ZHe data predicted significantly different pre-middle Paleogene thermal histories than both inverse models of proximal samples expected to share a similar thermal evolution (TUB15-05 and TUB15-06) and models from the same samples that excluded ZHe data. These samples were then rerun with an additional time-temperature constraint between 70-50 Ma to test if the ZHe data from these samples were consistent with a similar period of Paleogene reheating predicted by their corresponding AFT data and the inverse models of neighbouring samples. Occasionally, the applied diffusion models were unable to reproduce the spread in observed ZHe or AHe data. In those cases, outputs from model runs that excluded those unreproduced data were preferred. Thermal history models of previously unpublished AFT data from Tanzania, by contrast, were generated using the MonteTrax software as described by Gallagher[172].

While in a few instances thermochronology data from outcropping crystalline basement rocks record periods of reheating in response to burial[41,42,67], thermochronology systems are in general more sensitive to cooling events[102,103]. Therefore, to address the inherent bias of the thermal history model compilation towards preferentially recording crustal cooling, the dataset also includes published burial history models generated from well data (Fig. 3). These data, by contrast, predominantly record periods of upper crustal heating during subsidence, sedimentation and heating.

The resulting collation presented here, which combines thermal history inversions of regional thermochronology data and burial history models of well data, reveals spatiotemporal trends in Afro-Arabia crustal thermal evolution. These are recorded as paleotemperatures and cooling rates on a per-million-year basis that generally reflect periods of diachronous exhumation and burial in response to nearly 500 million years of tectonism.

Regional Trends in Thermochronology Data

The myriad of Phanerozoic upper crustal thermal fluxes recorded by low-temperature thermochronology of rocks at or near the Afro-Arabian surface are heterogeneously preserved across the geological landscape. A specific thermochronology system tends to preserve just one interval of an individual crustal block's long-term thermal history, restricted to recording the interval since those rocks last cooled below the upper limits of that system's particular thermal sensitivity. Yet, by employing multiple thermochronometers over the same region, a more complete thermal evolution can be recovered which documents those rocks having cooled through temperatures common in the upper ~10 km of the crust over tens to hundreds of millions of years.

The spread in thermochronology data is uneven across eastern Africa and Arabia, however, with analyses primarily limited to areas of exposed Precambrian crystalline igneous and metamorphic rocks (Figs. 4 & 5). This is by necessity as the largely mafic Eocene-recent volcanic assemblages that cover much of East Africa and southern Arabia[8,21] are usually devoid of the low-temperature thermochronology target accessory minerals of titanite, zircon and apatite, while younger Mesozoic-Cenozoic clastic sediments common throughout the region tend to retain the mixed thermal history signature of their provenance sources that are difficult to untangle[41,95].

The distribution of thermochronology data types is also unbalanced, with AFT data representing a disproportionately large percentage of the total existing analyses and present in virtually every thermochronology study across the region (Figs. 6 & 7). This is in general a reflection of the fact that the AFT system remains the best understood and consequently most commonly used low-temperature thermochronometer in geoscience today. Yet over the last decade as our understanding of the (U-Th)/He system has advanced significantly, the ZHe and AHe methodologies have become increasingly utilised in the region, to the point that we can also discuss macro-scale trends in these data across Afro-Arabia (Fig. 7). The use of the higher temperature ZFT, TFT and THe systems has nevertheless remained limited, with such data being largely reported from northern Mozambique, Madagascar, the northern Red Sea and Oman (Figs. 6 & 7).

Despite these limitations, the continental-scale multi-thermochronometer database presented here provides an invaluable record of the thermo-tectonic evolution of Afro-Arabia. While a detailed analysis of the tectonic and thermal events which Afro-Arabian thermochronology records is outside the scope of this Data Descriptor article, here we describe the regional trends in fission-track and (U-Th)/He data and allude to apparent anomalies which might warrant further investigation.

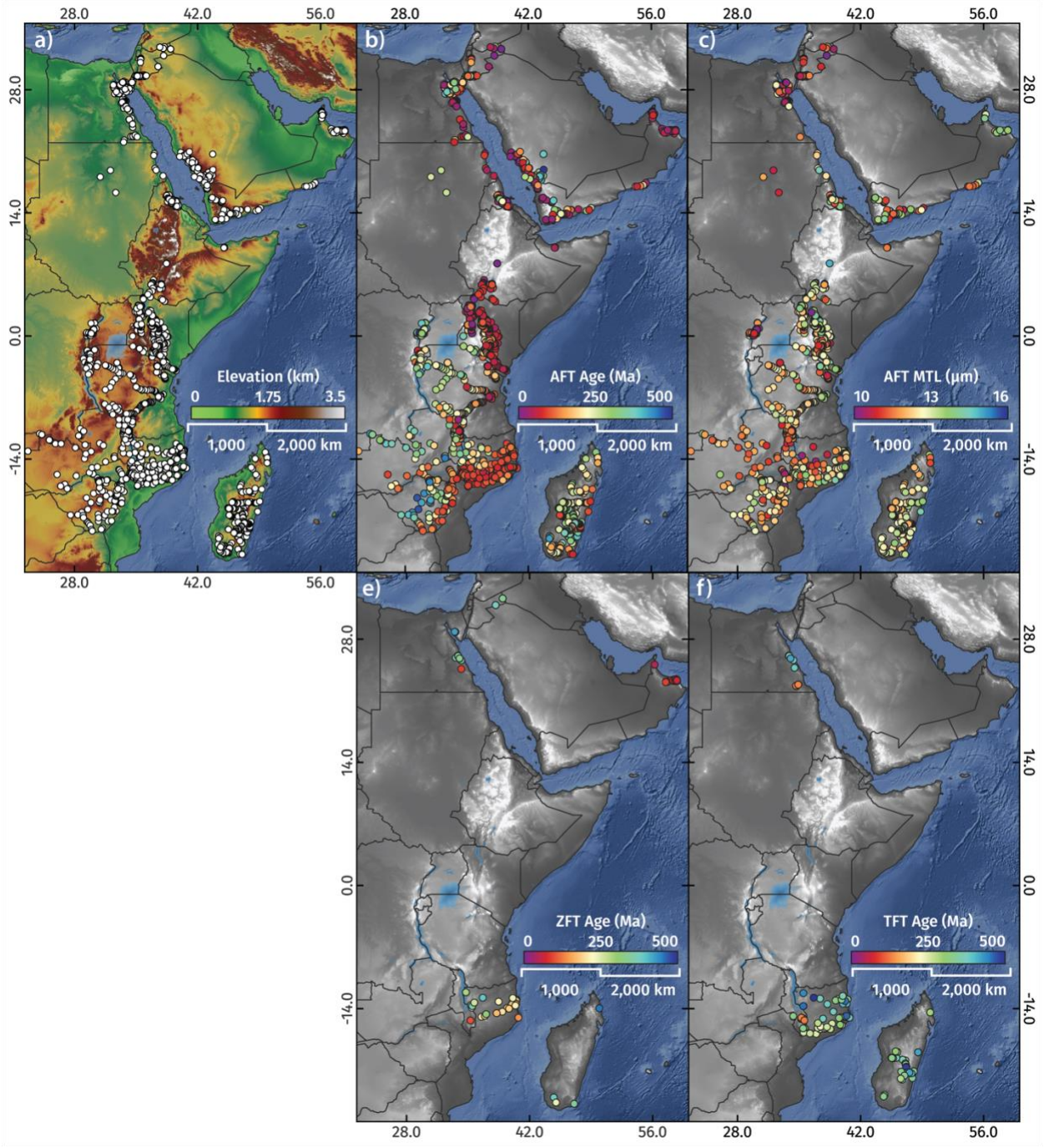

Figure 6. Fission-track data localities (a), apatite fission-track ages (b) and mean confined track lengths (c), zircon fission-track ages (d) and titanite fission-track ages (e) in the greater AARS region.

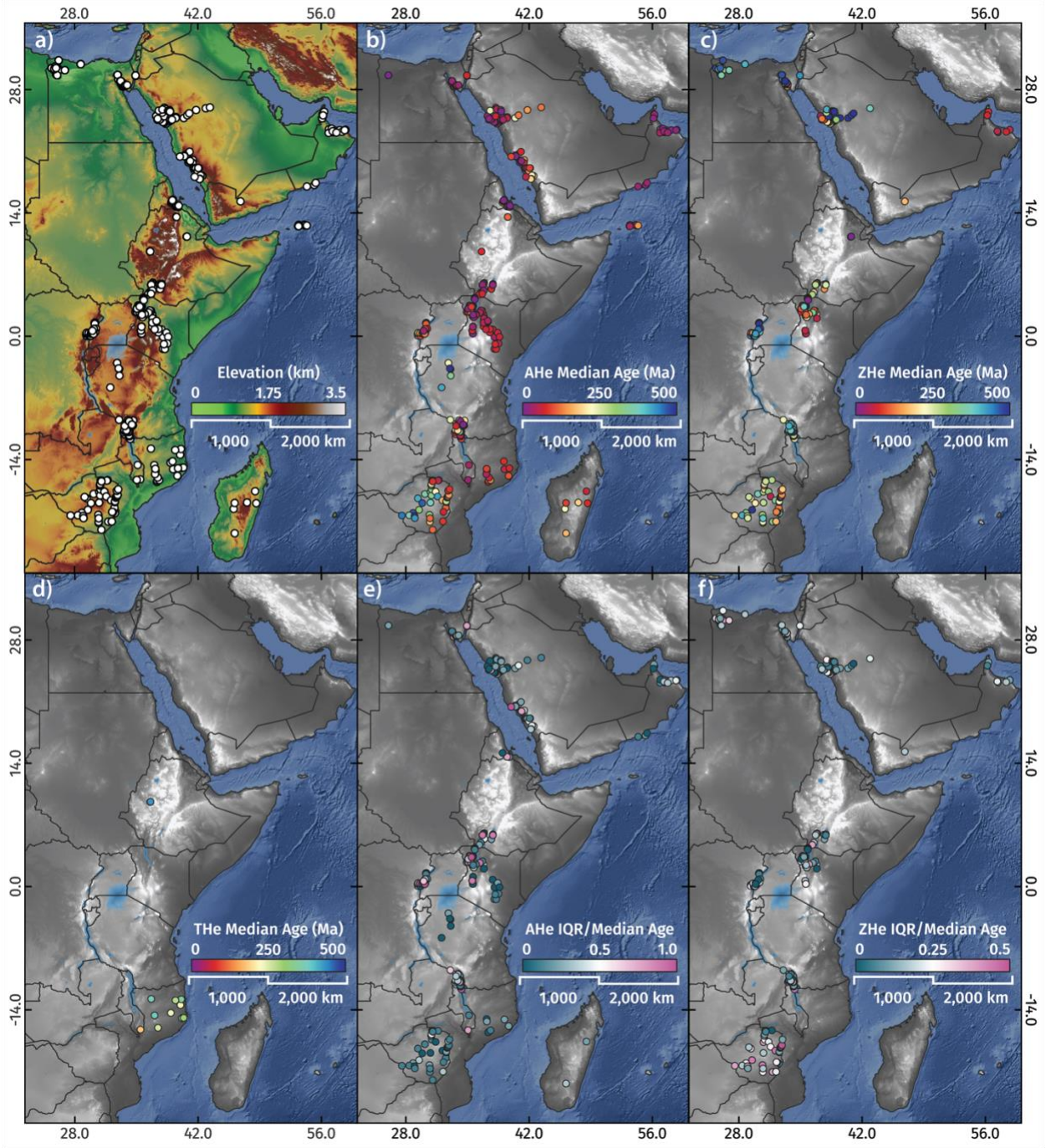

Figure 7. (U-Th)/He data localities (a), median apatite (U-Th)/He ages (b), median zircon (U-Th)/He ages (c), and median titanite (U-Th)/He ages (d) in the greater AARS region. Relative dispersion of apatite and zircon (U-Th)/He datasets are illustrated in (e) and (f), respectively, as single grain (U-Th)/He interquartile ranges divided by median ages.

TFT, THe, ZFT and ZHe data and insights into mid-crustal cooling

Higher temperature thermochronometers, such as TFT (~310-250 °C[144]), ZFT (~350-200 °C[145,146]), THe (~220-100 °C[168]) and ZHe (~210-180 °C, but sometimes as low as 35 °C for high radiation damage grains[63,108]), provide tools with which to constrain the thermal evolution of Afro-Arabian rocks through temperature regimes commonly found in the middle crust. By making interpretations about observed cooling recording advection of mass and heat towards the surface and making assumptions about paleogeothermal gradients, first-order paleo-exhumation estimates can be calculated. If, for example, a paleo-geothermal gradient of 25-35 °C/km is assumed (consistent with the average geothermal gradients of Archean-Proterozoic shields and mobile belts in East Africa, Nyblade[173]) and an average paleo-surface temperature of 20 °C, TFT ages can roughly be interpreted to represent when a sample exhumed through depths of ~11.6-6.6 km, ZFT ages as the timing of exhumation through depths of ~12-4.6 km, THe ages as corresponding to depths of ~8-2.3 km, and low radiation-damage ZHe ages as recording exhumation through depths of ~7.6-4.6 km.

While only a handful of studies have applied the TFT, THe and ZFT techniques in eastern Africa and Arabia[40,44,174–178,45,53,73,75,78,82,85,97], these coupled with the far more numerous analyses from the ZHe system of comparable temperature sensitivity still grant insights into the timing of mid-crustal exhumation of rocks now at the surface. However, interpretation of ZHe ages across Afro-Arabia can at times be challenging due to large intrasample single-grain ZHe age dispersion, primarily controlled by the effects of alpha recoil radiation damage accumulation, which at high levels can significantly increase radiogenic He diffusivity and decrease effective temperature sensitivity[108]. This is particularly problematic for old terranes with complex thermal histories, such as in northern Kenya and Zimbabwe, where current zircon radiation damage accumulation and annealing models are currently unable to reproduce the observed behaviour in ZHe data[41,63]. Though there are also multiple other factors that can increase intra-sample dispersion, such as grain chemistry, size and morphology[103]. The degree of intra-sample dispersion in (U-Th)/He datasets can nevertheless provide useful information for assessing the rate of cooling of a rock through the respective He partial retention zone[43]. This is because the slower a sample cools through a particular system's thermal sensitivity range, the more time there is for single-grain ratios of radioactive to radiogenic isotopes to diverge due to intrasample differences in grain characteristics and accumulated radiation damage. Thus, intrasample ZHe age dispersion, as quantified by the inter quartile range (IQR) normalised to a sample's median age (Fig. 7), can act as a first-order approximation for the rate of cooling through the temperature sensitivity range of a particular system[43]. In other words, more slowly cooled samples are more likely to have a higher single-grain (U-Th)/He age IQR, and vice versa.

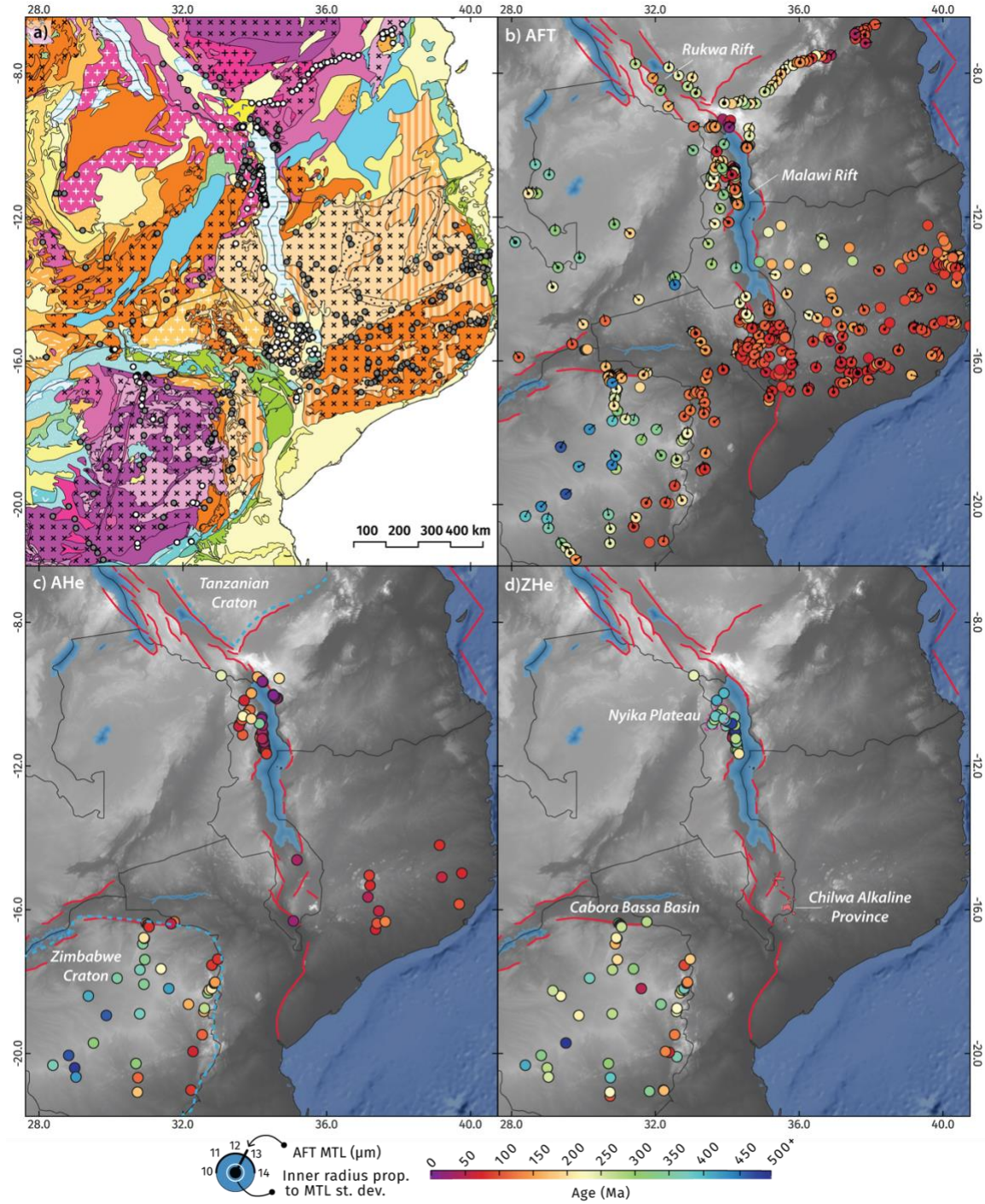

Figure 8. Maps of the southern Western Branch of the East African Rift System and Zimbabwe Craton region showing the distribution of previously published and unpublished thermochronology sample localities (a), and the trends in apatite fission track (b), apatite (U-Th)/He (c) and zircon (U-Th)/He data (d). Mean track lengths (MTLs) in panel (b) are represented using the 'tadpole' symbology of McMillan et al. (2022), with the tail orientation representing the MTL and the diameter of the inner circle being relative to MTL standard deviation (see key). Geological base map sourced from Thiéblemont et al.[27]. Refer to Figure 4 for geological map legend.

Zimbabwe Craton

Many of the oldest thermochronology ages (ZHe single grain ages up to 874 ± 54 Ma[63]) in all of eastern Africa and Arabia have been documented in the Archean Zimbabwe Craton. At first glance, ZHe data from Zimbabwe are confoundingly dispersed (Figs. 7 & 8). However, careful work by Mackintosh et al.[63–65] has placed these data in their geological context and performed robust thermal history modelling to make sense of these ages. In general, older (low radiation damage) ZHe ages from the central Zimbabwe Craton record a major period of Neoproterozoic-Cambrian deep-seated exhumation likely related to the coeval the ~650-550 Ma East African Orogen[23], and subsequent early Phanerozoic cooling possibly related to post orogenic collapse (Figs. 9 & 10). Thus, it remains possible that this latter period of cooling could, in part, record glacial exhumation related to a concurrent short-lived period of Late Ordovician glaciation which affected southern Africa circa 445 Ma[179].

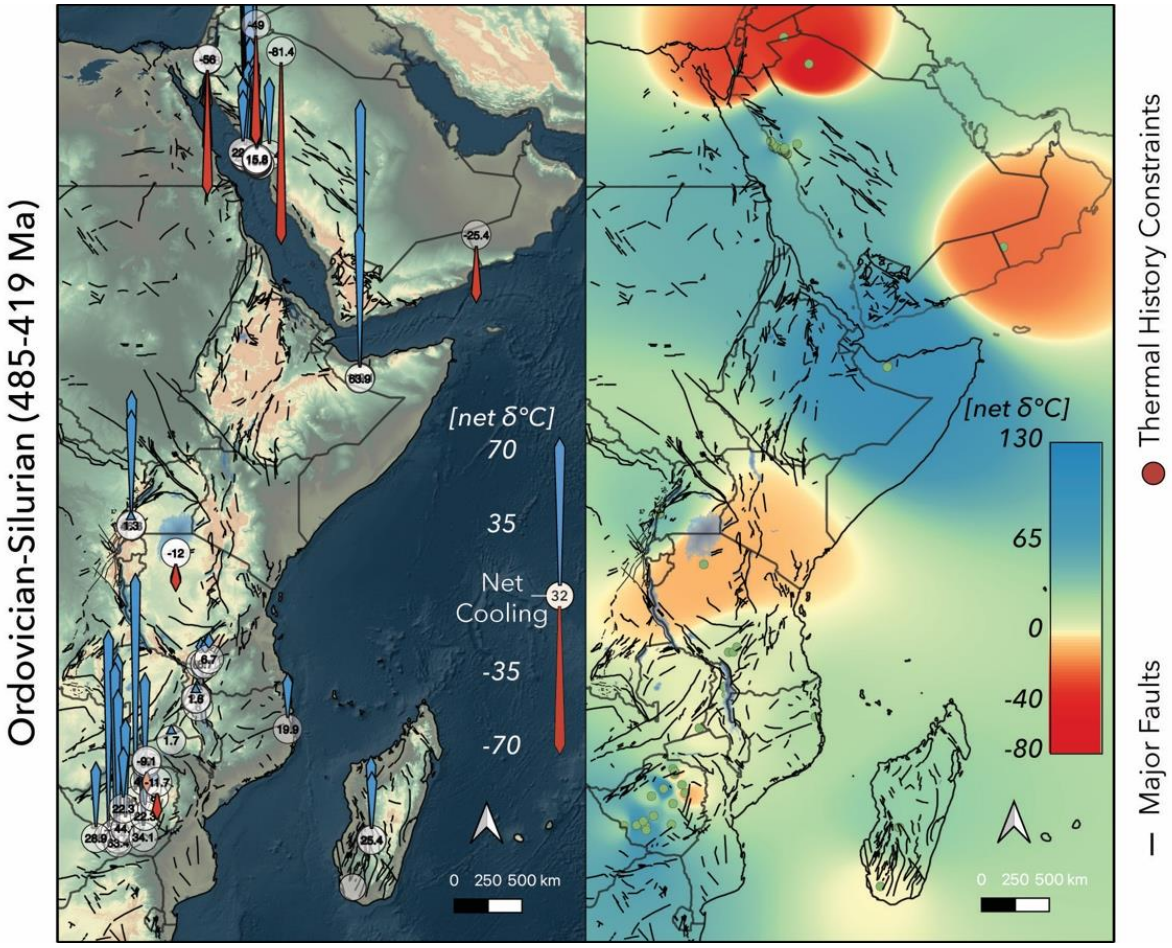

Figure 9. Regional patterns in Ordovician-Silurian upper crustal thermal histories as recorded by time-temperature models of thermochronology data and burial history models of well data, illustrated as proportionally sized cooling-heating arrows (left column) and as an inverse distance weighted interpolation (right column). Note the differences in scales between the interpolations for each range in geological time.

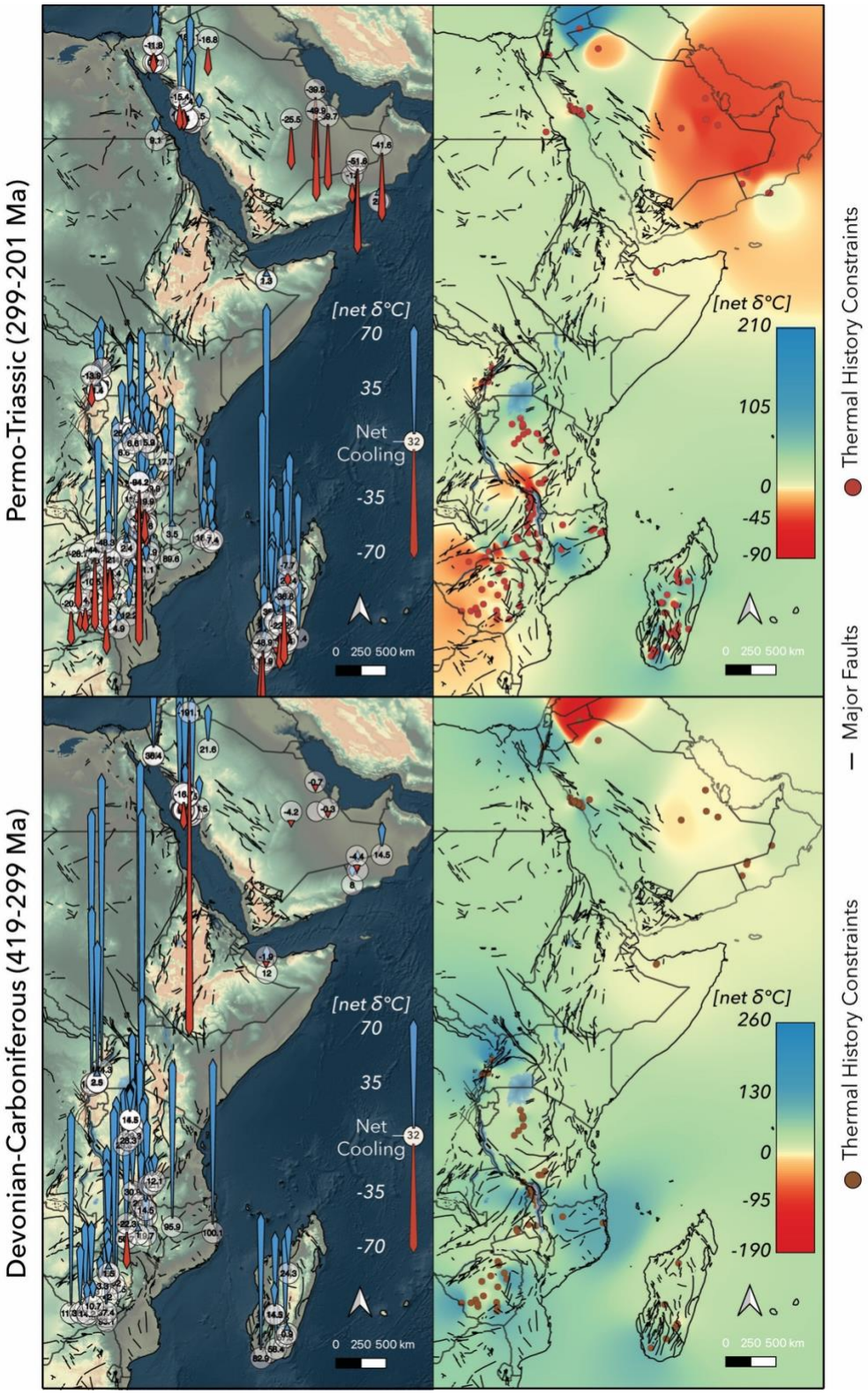

Figure 10. Regional patterns in Permo-Triassic (top panel) and Devonian-Carboniferous (bottom panel) upper crustal thermal histories as recorded by time-temperature models of thermochronology data and burial history models of well data. See Figure 9 for description of symbology. Note the differences in scales between the interpolations for each range in geological time.

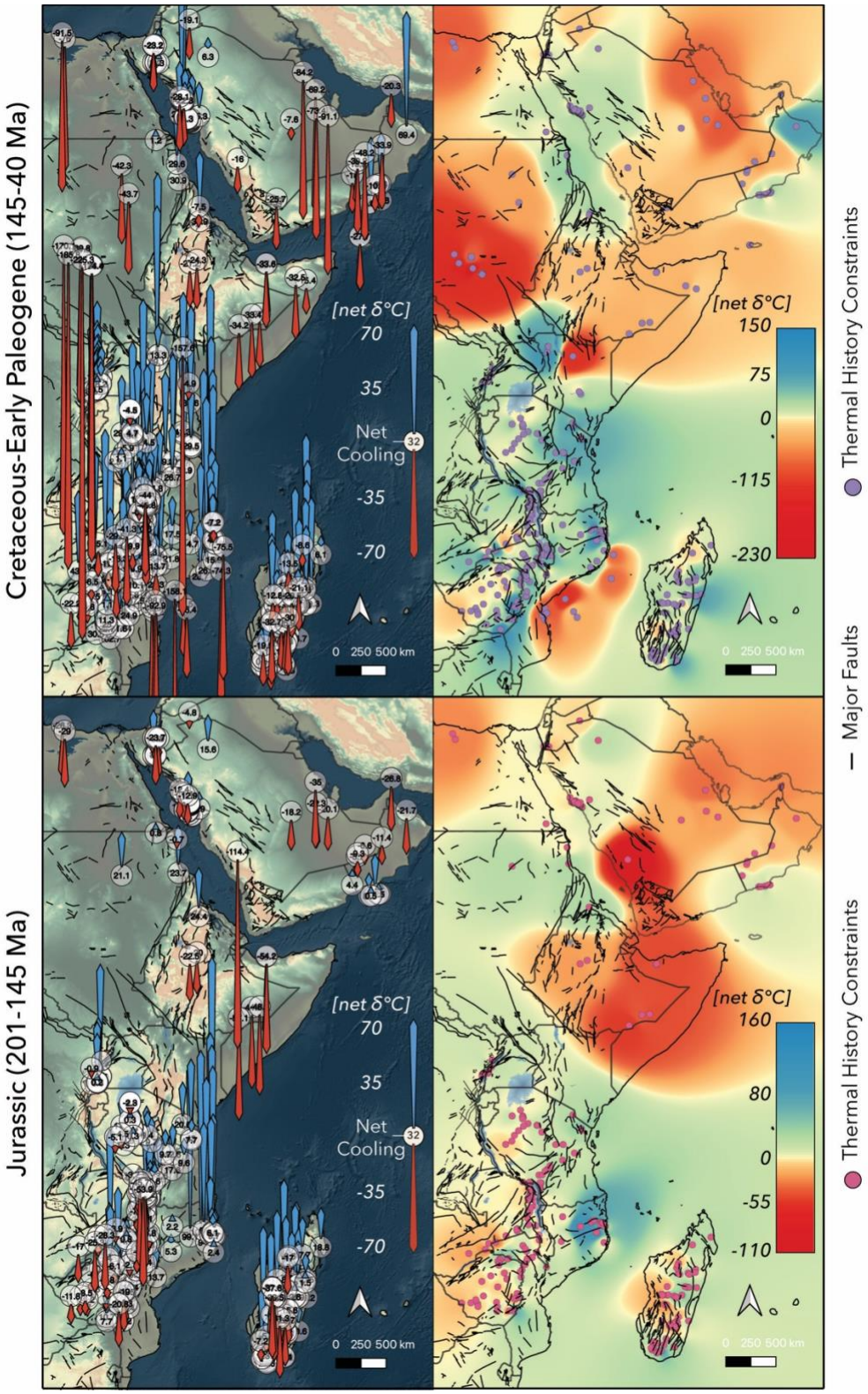

Figure 11. Regional patterns in Cretaceous-Early Paleogene (top panel) and Jurassic (bottom panel) upper crustal thermal histories as recorded by time-temperature models of thermochronology data and burial history models of well data. See Figure 9 for description of symbology. Note the differences in scales between the interpolations for each range in geological time.

Along the eastern Zimbabwe cratonic margin, ZHe data record pronounced periods of denudational cooling first during the Late Devonian-Carboniferous coeval with the early stages of widespread Karoo-aged rift basin development and glaciation recorded throughout much of southern and eastern Africa[1,179,180] (Fig. 10), and then in the Jurassic-Cretaceous during rifting of Antarctica from the southeastern margin of Africa[2,181] and subsequent development of the eastern passive margin of Africa (Fig. 11). Collectively, this is thought to have resulted in ~800 m of uplift of the southern Eastern Highlands of Zimbabwe[65]. Since then, rocks of the Eastern Highlands, now exposed at the surface, have remained relatively close to the surface (< 60 °C). Along the northern margin of the Zimbabwe Craton and within the Zambezi Belt, ZHe data record Late Carboniferous denudation in response to rifting and formation of the Karoo-aged Cabora Bassa Basin[64] (Figs. 8 &10).

East African Margin and Mozambique

In the northern-most part of Mozambique, TFT and ZFT data show a gradual younging trend from middle Palaeozoic ages in the west to late Paleozoic-early Mesozoic towards the east (Fig. 6). This trend is overprinted by a transition to even younger Permo-Triassic ages heading south towards the ~SW-NE trending coast of central Mozambique. THe data exhibit a similar NW-SE younging trend from Devonian ages in the hinterland towards Triassic-Jurassic ages nearer the Mozambican coast, with the shift to younger ages correspondingly to a change from the moderate topography of inland Mozambique to the flat, low-lying coastal plains (Fig. 7). The spatial distribution suggest they may record exhumation from mid to upper crustal depths in the Triassic-Jurassic, possibly related to the rifting of Antarctica and Madagascar from southern Africa at that time[2,182].

The longer wavelength trend of older Paleozoic mid-temperature thermochronology ages in the hinterland is interrupted by an isolated cluster of younger Cretaceous TFT and ZFT ages from the Chilwa alkaline province of southern Malawi which intruded into crust at that time. It is thought that Chilwa magmatism was caused by crustal extension, which ruptured pre-existing zones of weakness and led to decompression melting[53]. But relatively little work has been done on these intrusions to pinpoint their geodynamic significance.

Madagascar

In Madagascar, TFT and ZFT data exhibit an opposite SE-NW younging trend, with ages transitioning from mid-late Palaeozoic along the eastern margin to Permian near the Mozambique Channel (Fig. 6). The lack of data near the west coast which is covered by Mesozoic sedimentary rocks (Fig. 4) precludes assessing whether this trend continues all the way to the Mozambique Channel. These ages have been interpreted to record a prolonged period of deep-seated Carboniferous-Triassic exhumation-related cooling associated with the broadly coeval formation of extensive, thick Karoo rift basins along the west Malagasy margin[175,183,184].

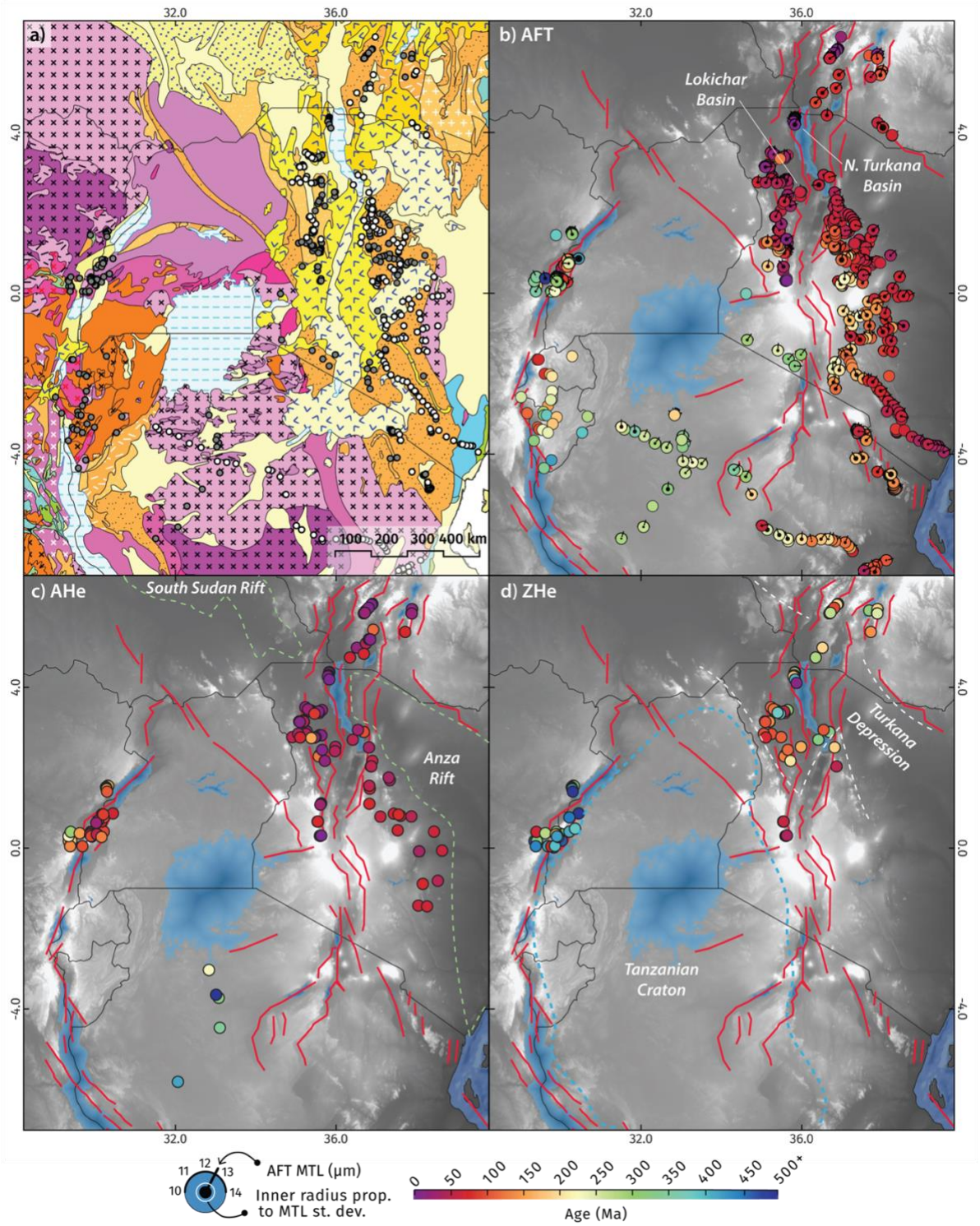

Figure 12. Larger scale maps of the Eastern and northern Western Branches of the East African Rift System showing the distribution of previously published and unpublished thermochronology sample localities (a), and the trends in apatite fission track (b), apatite (U-Th)/He (c) and zircon (U-Th)/He data (d). Refer to the Figure 8 caption for a description of the MTL 'tadpole' symbology. Geological base map sourced from Thiéblemont et al.[27]. Refer to Figure 4 for geological map legend.

Western Branch of the EARS

ZHe data in the Western Branch of the EARS are confined to northern Malawi and along the Uganda-Democratic Republic of Congo border region (Figs. 7, 8 & 12). In Malawi, Silurian to Carboniferous ZHe ages are distributed across the ~2500m high Nyika Plateau, with the youngest ages preserved in the highlands (Fig. 8). Thermal history modelling of these data by McMillan et al.[67] revealed that rocks now exposed on top of Nyika experienced pronounced Permo-Triassic cooling while samples from the neighbouring modern lowlands were being buried and reheated beneath Karoo sediment, leading them to argue that the Nyika Plateau formed as an isostatically uplifted horst.

ZHe data from Uganda and eastern DRC record prolonged gradual cooling in the Ordovician-Silurian, the cause of which is poorly understood. One hypothesis proposed by Bauer et al.[35] is that this region may have acted as a long-lived sediment source area for the neighbouring intracontinental Congo Basin, which preserves enormous volumes of early-middle Paleozoic sediment that were deposited during interspersed periods of Cambrian-Ordovician East African Orogen unroofing and regional Ordovician-Silurian glaciation[179,185,186]. However, the high degree of intrasample single-grain ZHe age dispersion, thought to be caused by varying degrees of radiation damage accumulation enhanced diffusivity[35], has thus far prevented the exact timing of Paleozoic cooling of the Ugandan-Congolese borderlands to be well constrained. Thus, the geodynamic drivers of proposed early-middle Paleozoic exhumation in this region remain enigmatic.

Turkana Depression

ZHe data from the Turkana Depression of northern Kenya and southern Ethiopia come from both Precambrian basement rocks and Cretaceous-Paleogene sandstone units, with single-grain ages ranging from Devonian to Quaternary (Figs. 7 & 12). ZHe data from Cretaceous-Paleogene sandstone units, thought to be deposited in a number of depocentres that once may have link the Cretaceous-Paleogene rifts of South Sudan to the similarly aged Anza Rift of Kenya[187,188], yield a wide range of Tonian-Cretaceous single-grain ZHe ages[41,42] (Fig. 13). These sedimentary rocks only appear to preserve zircon grains of low to moderate (40.0-1069.2 ppm) eU concentrations ($eU = U + 0.235 \cdot Th$), a proxy for radiation damage accumulation (Flowers et al., 2023). This suggests that grains with higher radioactive chemistries, and thus more likely to have become metamict, did not survive pre-depositional sediment transport. Basement rocks from northern Kenya and southern Ethiopia, on the other hand, yield younger ages between 450-1 Ma, corresponding to a much broader range of eU content (1.6-16027.7 ppm)[41,42,86] (Fig. 13). This clear divergence between single grain ZHe age spectra observed in Proterozoic basement rocks and those in Cretaceous-Paleogene sedimentary rocks invokes two potential Phanerozoic intra-African source-to-sink scenarios. Either the older Tonian-Ordovician ZHe ages preserved in Cretaceous-Paleogene successions of the Turkana Depression were sourced from a distal source elsewhere in Africa or the basement rocks from central Kenya and southern Ethiopia which may have once recorded similarly old ZHe ages have since been eroded away. Both scenarios have important ramifications for the tectono-stratigraphy of the region, warranting further investigation into the marked contrast between detrital and basement ZHe data in the Turkana Depression.

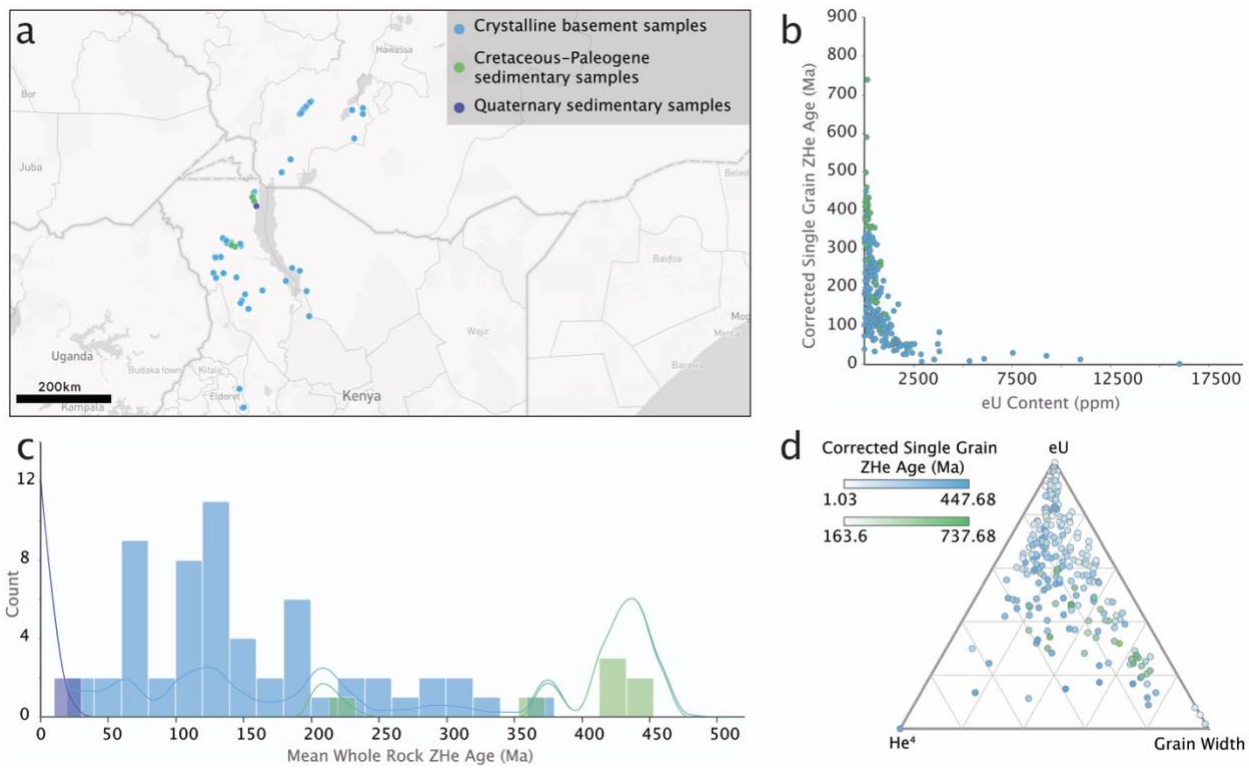

Figure 13. Zircon (U-Th)/He data from the greater Turkana Depression region. (a) Locations of samples from northern Kenya and southern Ethiopia. (b) Single grain ZHe ages versus effective uranium (eU = U + 0.235·Th), a proxy for radiation damage accumulation. (c) Histogram and kernel density estimates of whole rock mean ZHe ages. (d) Ternary plot of single grain ZHe data showing relative eU content, radiogenic 4He and zircon crystal width, coloured by corrected single grain ages. Map and plots generated in EarthBank[100,101].

Taken separately, ZHe ages recorded in Precambrian basement rocks in Kenya and southern Ethiopia record highly dispersed single grain ages, which for the most part negatively correlate with eU content (Figs. 13 & 14). In some instances, individual crystalline rock samples yield an extreme range in eU content and thus ZHe ages. For example, sample TUB13-55 from Kenya yields grains ranging from 322.4 ppm eU and an age of 274.2 ± 17.0 Ma to 2166.4 ppm eU and a 37.6 ± 2.3 Ma age (Fig. 15). The wide ranges in accumulated radiation damage and breadth of resulting effective temperature sensitivities of zircon grains within samples like this provide an amazing opportunity to extract large portions of the pre-EARS Phanerozoic thermo-tectonic evolution of this region. In particular, these data may record conductive changes in crustal geotherms during pre-EARS crustal thinning (Fig. 14), considered so important for governing the subsequent regional response to EARS rifting[5,189,190], but for which the spatiotemporal chronology remains poorly understood[41]. However, limitations in the ability of existing zircon radiation damage accumulation and annealing models to reproduce observed ranges in intrasample single grain ZHe ages[41,63] have hindered attempts to quantify the time-temperature evolutions which these data record via thermal history modelling. As new zircon radiation damage models are developed in the future, renewed interrogation of this dataset is warranted.

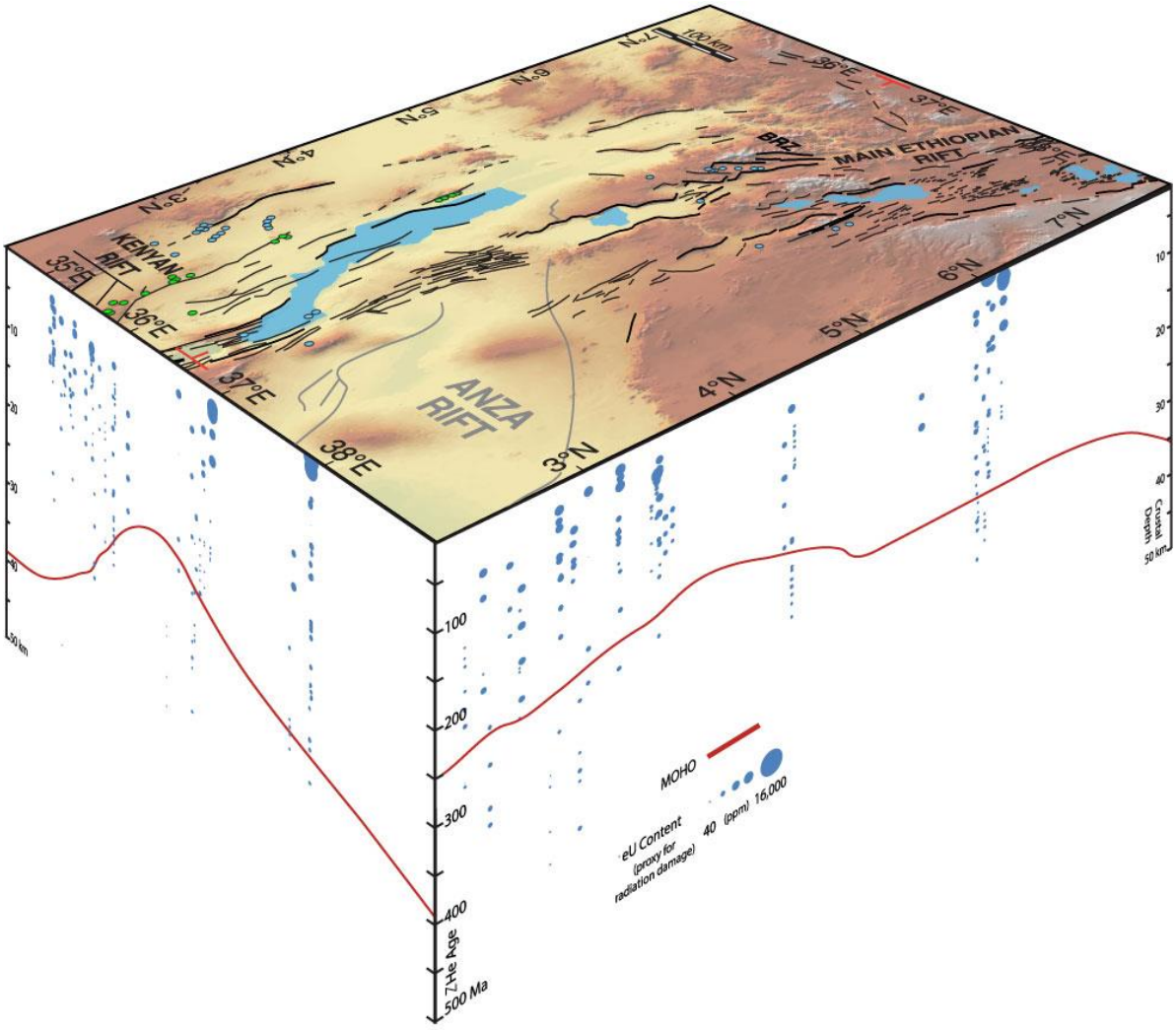

Figure 14. Longitudinal and latitudinal trends in single-grain ZHe age versus effective uranium content (eU; corresponding to circle size) for Turkana Depression Precambrian basement rocks. Surface panel shows distribution of sample locations (previously published in green, previously unpublished in blue), major Cretaceous-early Paleogene Anza Rift faults and major late Paleogene-Quaternary EARS faults[27,137,191] on a digital elevation model. Longitudinal and latitudinal Mohorovičić (MOHO) discontinuity profiles[17] are shown for 2° N and 36.5° E, respectively.

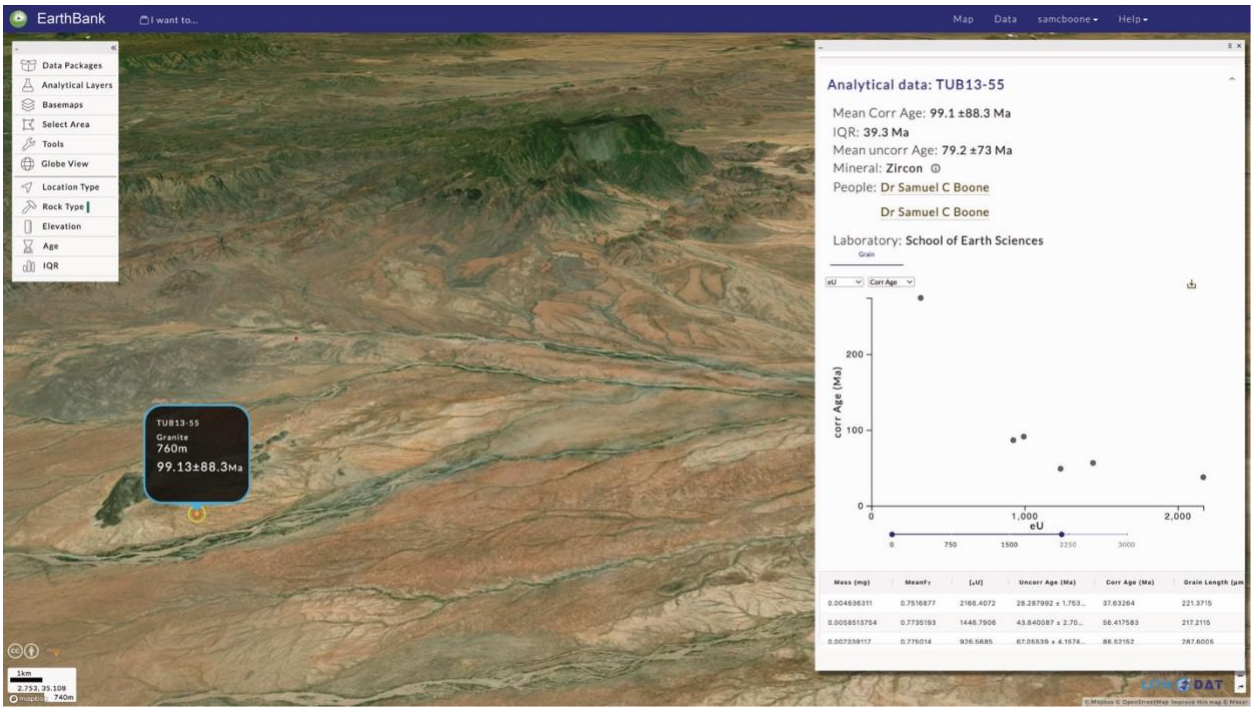

Figure 15. Zircon (U-Th)/He data from granite sample TUB13-55 viewed in EarthBank (previously AusGeochem[100,101]), showing significant intra-sample dispersion in single grain ZHe ages and eU content.

Red Sea Margin

TFT and ZFT data from the wider Red Sea area are restricted to outcrop samples from along its northeast margin and the Sinai Peninsula, and from boreholes in northern Arabia (Fig. 6). TFT and ZFT ages are largely Silurian to Carboniferous (315 ± 27 to 422 ± 37 Ma) and thought to record as much as 10 km of Devonian-Early Carboniferous denudation due to some combination of Gondwana-Laurasia collision and Paleo-Tethyan Ocean subduction[40,73,93]. Only TFT and ZFT data from the central western Red Sea margin yield younger ages, which are coeval with Cretaceous alkaline igneous activity in the area[75].

ZHe data are far more numerous in the region but remain largely restricted to three areas: the eastern margin of the Gulf of Suez, the central Red Sea escarpment in western Arabia, and the Western Desert of Egypt (Figs. 7 & 13). ZHe data in the hinterlands of Arabia and the Sinai Peninsula are highly dispersed, with ages ranging from Ediacaran to Jurassic. When interpreting the geological implications of these ages, authors have previously pointed to a breadth of regional Paleozoic-Mesozoic tectonic events which could plausibly have resulted in deep-seated exhumation in Arabia. Yet, it remains unclear whether ZHe data from outcropping bedrock in these regions could really preserve the erosional cooling signature of the numerous thermo-tectonic events proposed to have affected Arabia, including Devonian-Carboniferous Hercynian orogenesis[73,84] and Pangean subduction dynamics[192], Devonian passive margin formation processes along northern Arabia[84], and Late Jurassic-Cretaceous rifting of Pangaea[84]. Further investigation into whether ZHe age dispersion could instead reflect the compounding effects of intragranular variability in He diffusivity (e.g., due to differences in radiation damage, grain

morphology, etc.) and differing degrees of denudational cooling during a single shared younger geological event is warranted. While an investigation into the geological drivers into the thermal histories recorded by these data is beyond the scope of this Data Descriptor article, a detailed synthesis of the current geological interpretations of these data can be found in Boone et al.[93] and the references therein.

In the Western Desert of Egypt, detrital ZHe ages from a series of wells that penetrate subsurface lower Paleozoic, Carboniferous and Mesozoic sedimentary sequences range from Paleoproterozoic to Cenozoic (Figs. 7 & 16). These zircons, thought to be locally sourced due to very small lag times between large peaks in detrital ZHe ages and stratigraphic ages of sampled sedimentary units, provide an invaluable archive of the complex tectono-stratigraphy of northern Gondwana for much of the Phanerozoic.

Along both the western margins of the Gulf of Suez and the Red Sea, outcropping basement rock ZHe ages progressively young from background Neoproterozoic-Paleozoic ages in the hinterland towards the rifted margins (Figs. 7 & 16). Along the central eastern Red Sea margin, mean ZHe ages drop to as young as 19.3 ± 1.0 Ma on the coastal plain, interpreted by Szymanski et al.[84] to record pronounced Miocene cooling associated with the extensional isostatic rebound and exhumation of the rifted margin during Red Sea rifting. In the Gulf of Suez, by contrast, ZHe data only reach mean ages as young as 147 ± 162 Ma along the coast, though single grain ZHe ages drop to as low as 18.4 Ma. This indicates that the eastern margin of the Gulf of Suez rift sector experienced reduced amounts of Miocene rift margin exhumation compared to that in the central Red Sea, where total extension rates are considerably higher.

Oman

Numerous authors have applied the ZFT and ZHe methodologies (along with AFT and AHe analyses described below) to disentangle the complex tectono-thermal evolution of Oman which involved Late Cretaceous ophiolite obduction onto the Arabian passive margin, isostatic rebound due to slab breakoff, and the subsequent Cenozoic collision of Arabia with Eurasia, the timing of which is disputed[55,56,81,82,85,193]. As reviewed by Boone, Balestrieri and Kohn[93], there currently remains no consensus on the geological interpretations of these ZFT (47 ± 4 Ma to 93 ± 4 Ma) and single grain ZHe ages (38.8 ± 1.9 to 81.0 ± 4.1 Ma) (Figs. 7 & 13). This is due to a series of compounding issues such as heterogenous data coverage along the margin, significant intra-sample ZHe dispersion resulting from a wide range of possible morphological, crystallographic and chemical factors[162,163,167], and the current lack of robust He diffusion models able to adequately account for these phenomena[63,194,195]. A more coherent understanding of the thermal evolution of the Omani margin might be obtained through a reassessment of the full regional dataset which involves re-running thermal history models using the same modelling codes and parameters.

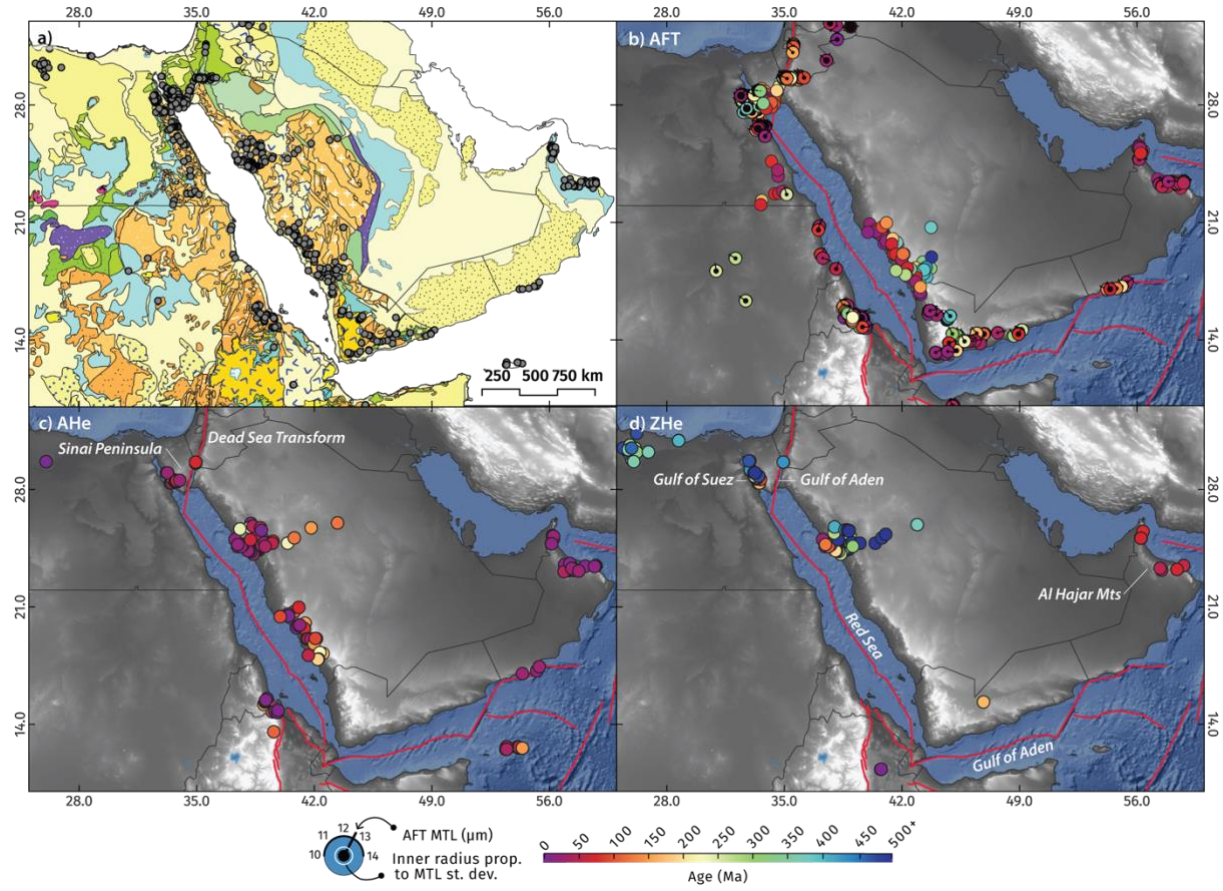

Figure 16. Larger scale maps of the greater Red Sea-Gulf of Aden region showing trends in apatite fission track (a), apatite (U-Th)/He (b) and zircon (U-Th)/He data (c). Refer to the Figure 8 caption for a description of the MTL 'tadpole' symbology. Geological base map sourced from Thiéblemont et al.[27]. Refer to Figure 4 for geological map legend.

AFT and AHe data and insights into upper-crustal cooling

The lower temperature AFT and AHe thermochronometers have been far more widely utilised across the greater AARS region (Fig. 6). The complementary and largely overlapping temperature sensitivities of the AFT (~110-60 °C[141]) and AHe (~80-40 °C[164]) systems make them invaluable tools for constraining the timing and rate of geological processes which change the thermal regime in the upper ~4-5 km of the crust over geological timescales[103]. While the time-temperature histories recorded by AFT and AHe data can in some cases reflect more transitory thermal mechanisms such as conductive heating by proximity to igneous activity[196], groundwater[197], hydrothermal fluids[86,198], or wildfires[199], in the majority of cases they record denudational cooling due to tectonic and/or erosional exhumation[102,103]. In extensional settings, like the AARS, these make them valuable tools for constraining the timing and rate of exhumation of normal fault footwalls in response to extension and, in some instances, subsidence and reheating of hanging walls due to syn-rift burial[111]. For basin-bounding faults where the rift margins have experienced sufficient amounts of denudational cooling in response to extension,

along-strike trends in footwall cooling can even be used to reveal the structural evolution of normal fault systems[43,68,71]. When collated with other independent geological observations, regional-scale AFT and AHe datasets can reveal spatiotemporal rifting chronologies of continental-scale rift systems that can provide powerful insights into rift inception, nucleation and propagation processes[5,93,99].

For whole-grain (U-Th)/He ages, the only type of (U-Th)/He data presented in this dataset, a wide variety of thermal histories can yield the same the ratio of radiogenic U and Th (and Sm in the case of AHe) to accumulated He[103], making them difficult to interpret in isolation. Fortunately, the vast majority of AHe data from Afro-Arabia are complemented by AFT data from the same rocks, making them the richest and most comprehensive thermochronology dataset in the region. In contrast to whole-grain (U-Th)/He analysis, AFT does not suffer from the issue of non-uniqueness to anywhere near the same degree. This is because in addition to an apparent age, the length distribution of confined fission tracks is measured, with the length of each individual fission track being proportional to the maximum temperature which that track has experienced since it formed[200]. Thus, the shape, mean track length (MTL) and spread of confined track distributions are diagnostic of the cooling path through the AFT PAZ.

Cratonic Interior

In general, background AFT ages of the East African hinterland are mid-Palaeozoic, centred on the Archean-Paleoproterozoic Zimbabwe Craton, Tanzanian Craton, and Bangweulu Block (Figs. 6, 8 & 12). These Palaeozoic ages of the hinterland are then interrupted by linear trends of younger, generally Permo-Triassic and Jurassic-Cretaceous AFT ages that coincide with the trends of the widespread Permo-Triassic Karoo Basins that formed throughout southern and eastern Africa during a period of prolonged continental-scale rifting[1]. Many of the fault systems which first formed during the Permo-Triassic and created the accommodation space in which Karoo-aged sediment were deposited were reactivated again in the Jurassic-Cretaceous during the breakup of Gondwana and subsequent formation of the passive East African margin[64]. The spatiotemporal trends in km-scale uplift and denudation recorded by these data may also have important implications for the long-term evolution of the interior drainage system of Africa. For example, sandstones from the Karoo Cabora Bassa Basin, immediately to the north of the northern Zimbabwe Craton record Late Triassic-Early Jurassic to Early Cretaceous cooling[64] that is interpreted to represent to a major drainage reversal circa 165 Ma of the Zambezi River from west- to east-flowing in response to Gondwana fragmentation[201].

Apatite (U-Th)/He data from the cratonic interior of East Africa display significant intra- and inter-sample age dispersion, corresponding with a wide range of eU concentrations (Fig. 17). Single grain AHe ages in the Zimbabwe and Tanzanian Cratons range from 18 ± 1 Ma[64] to 701 ± 96 Ma[58] with no clear relationship to eU content (Fig. 17), suggesting other factors such as crystal size, grain morphology, intracrystalline geochemical heterogeneity or He trapping in crystal defects and vacancies may also play a role in driving dataset dispersion[103]. Nevertheless, a positive correlation between mean AHe ages and elevation (Fig. 17), consistent with cooling histories driven by exhumation, attest to the geologically significant time-temperature histories which these data record. Yet, further work is required to fully disentangle the range of factors

known to cause excess AHe age dispersion in slowly cooled cratonic terranes[103,162] from the regional upper crustal thermal evolution obscured in this complex dataset.

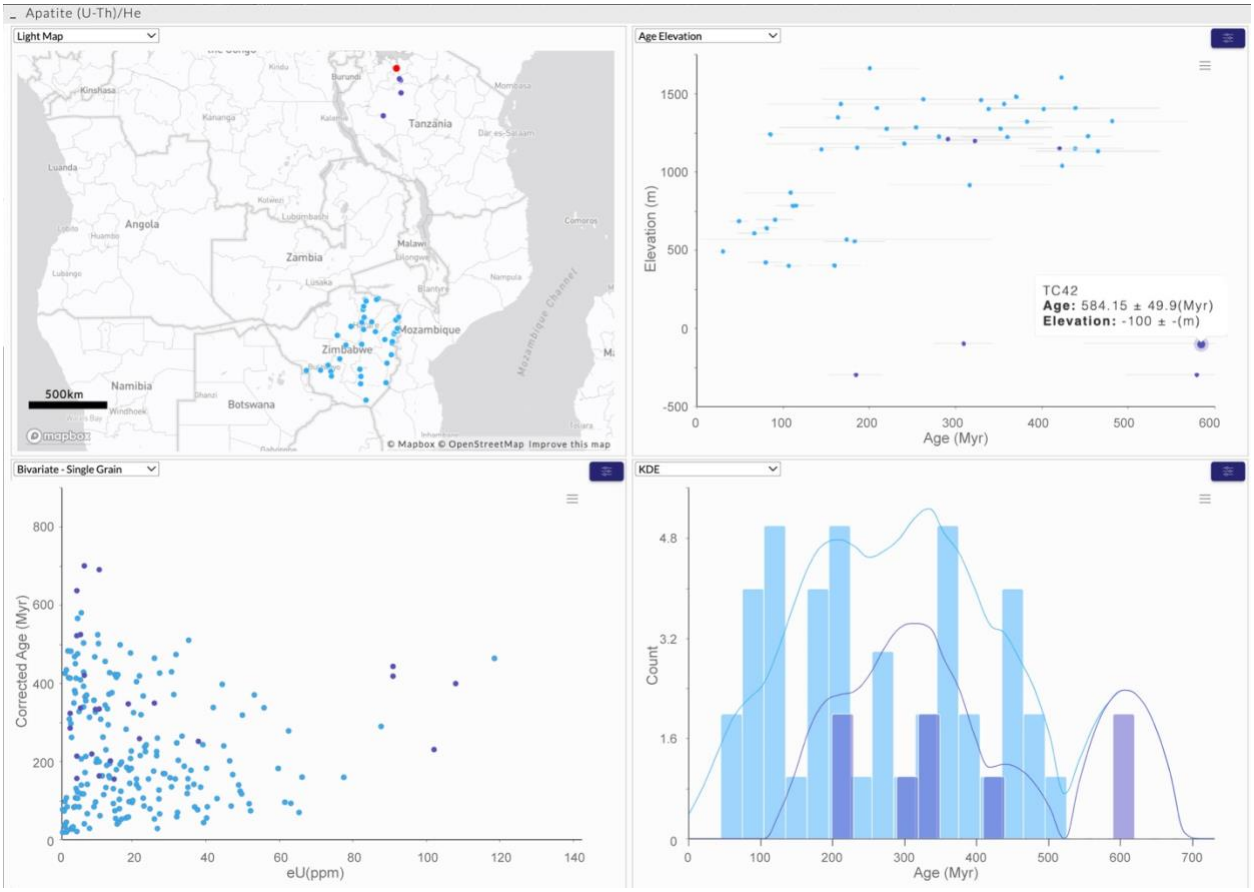

Figure 17. Apatite (U-Th)/He data from the Zimbabwe (blue circles) and Tanzanian Cratons (purple circles). Sample localities (top left), mean AHe ages versus elevation (top right), single grain AHe ages versus eU content (bottom left), and a kernel density distribution of mean AHe ages are shown in an EarthBank dashboard (previously AusGeochem[100,101]).

East African Margin

Heading east towards the coast, AFT ages sharply transition towards younger Cretaceous ages on the East African margin of Mozambique and Tanzania, and even down to as young as early Paleogene in eastern Kenyan (Figs. 6, 8 & 12). The widespread occurrences of these young, Cretaceous-early Paleogene ages and their distribution along the coastline suggest these record cooling associated with a long wavelength geological mechanism(s) operating at that time. Interestingly, these ages significantly postdate the Jurassic rifting of Madagascar and Antarctica away from East Africa[2], and thus require an alternative post-breakup mechanism for driving the widespread pronounced denudation which they record. Temporal and spatial decoupling of passive margin evolution and crustal denudation recorded by thermochronology data have been reported from other Gondwana rifted margins, with continental breakup-induced mantle

convection instabilities[202] and removal of onshore low-thermal conductivity sedimentary basins[203] inferred as potential causal mechanisms.

Madagascar

In Madagascar, background AFT ages are also mid-late Palaeozoic. AFT ages then decrease towards the southern and eastern margins of Madagascar to Jurassic and Cretaceous ages, respectively (Fig. 6). One possibility is that these relate to rifting of first Antarctica (Early Cretaceous) and then India (Late Cretaceous) from Madagascar. However, when viewed in their pre-Gondwana-breakup palinspastic context, this trend of Late Cretaceous apparent ages along Madagascar's east coast continues uninterrupted to the southwest along what is today the Mozambique passive margin (Fig. 18). While this could simply be fortuitous, it may be worth exploring other mechanisms which might have resulted in widespread Late Cretaceous cooling along the eastern margins of both Mozambique and Madagascar well after the breakup of central Gondwana. One such mechanism could be contemporaneous dynamic topography development and major changes in relative Africa-Madagascar-India plate motions linked to the arrival of the Morondova Plume circa 105 Ma[204].

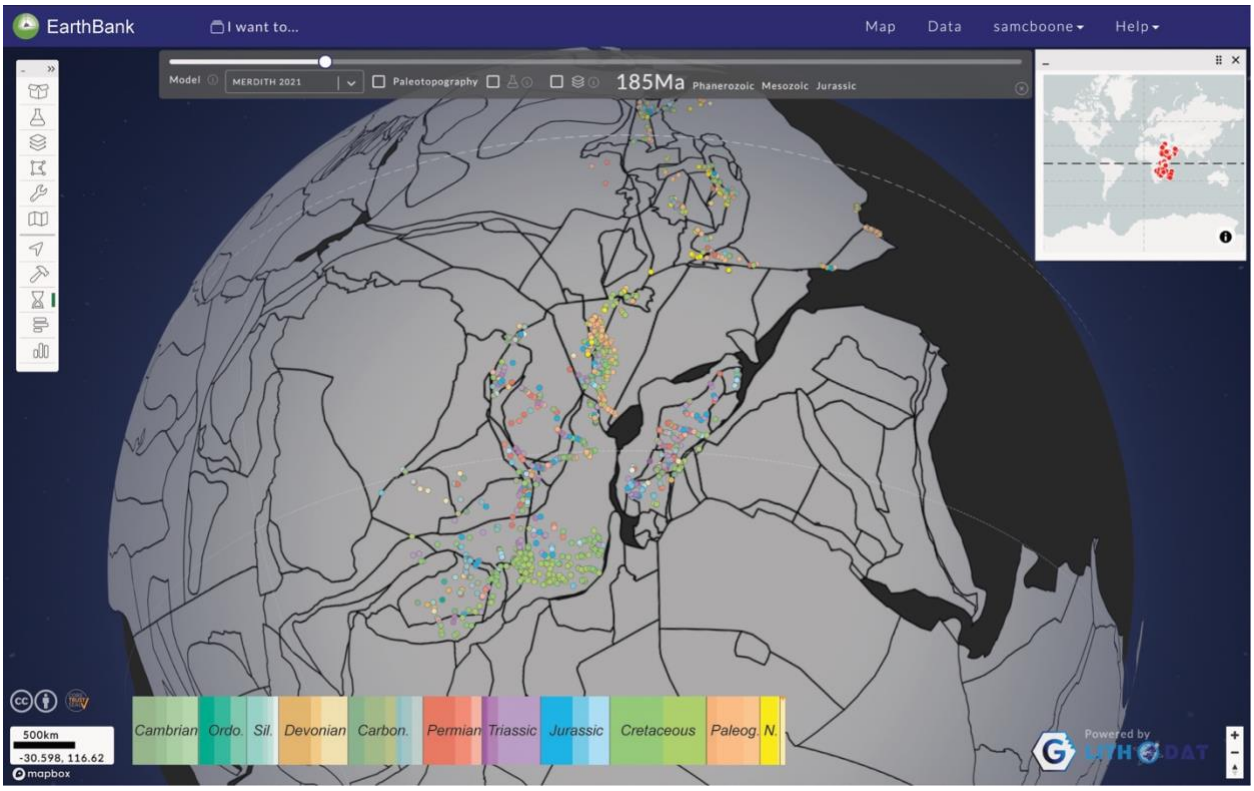

Figure 18. AARS apatite fission-track data in their 185 Ma paleogeographic context. Note, when viewed in this plate reconstruction context, the trend of Cretaceous AFT apparent ages (green dots) along eastern Mozambique continues to the northeast along what is today eastern Madagascar. Data were reconstructed according to the Merdith et al.[181] plate tectonic model in the open-access EarthBank data platform (previously AusGeochem[100,101]).

Interestingly, Jurassic breakup of Madagascar from East Africa is not clearly recorded in the AFT age trends from western and north-western Madagascar. However, this may be due to a ~100-300 km data gap running along the west and northwest coasts of the island where the basement is covered by Permian-Jurassic onshore rift sediments (Fig. 4). It is therefore possible that this Jurassic denudation signal may be preserved in basement rocks at depth and obscured by the overlying sedimentary successions.

Anza Rift

AFT ages decrease northwards towards Kenya and southern Ethiopia, where the predominant signal in apparent ages is Cretaceous-Paleogene along both sides of the NW-SE trending Cretaceous-Paleogene Anza graben (Fig. 12). Many authors have interpreted this widespread period of Cretaceous-early Paleogene cooling as recording syn-rift uplift and denudation of the Anza rift margins[49,50,74,86]. Yet, it remains unclear how flexural isostatic rift margin uplift in response to extension, normally restricted to the immediate footwall regions of major basin-bounding fault arrays[205], could have been responsible for driving km-scale denudation as much as 200 km away from the Anza graben. Thus, future studies might consider the role of alternative mechanisms, such as edge-driven mantle convection or paleoprecipitation flux, in amplifying denudation of the Anza Rift hinterland.

AARS Basins and Rifted Margins

AFT and AHe data trends along the AARS (Figs. 6, 7, 8, 12 & 16) reflect a combination of rift maturity, structural geometry, and geothermal regime, intrinsically linked to lithospheric architecture and magmatic activity. These relationships are best illustrated by contrasting the upper crustal thermal evolutions of different AARS segments of varying age and complexity. For example, between the nascent Okavango and the mature Ethiopian and evolved Red Sea rifts, between wide (e.g. Turkana Depression) versus narrow (e.g. Main Ethiopian Rift) zones of deformation, between areas of transtensional (Dead Sea Transform), oblique (e.g. Gulf of Aden) and sub-orthogonal rifting (e.g. Malawi Rift); and between the magmatic eastern versus amagmatic western branches of the EARS.

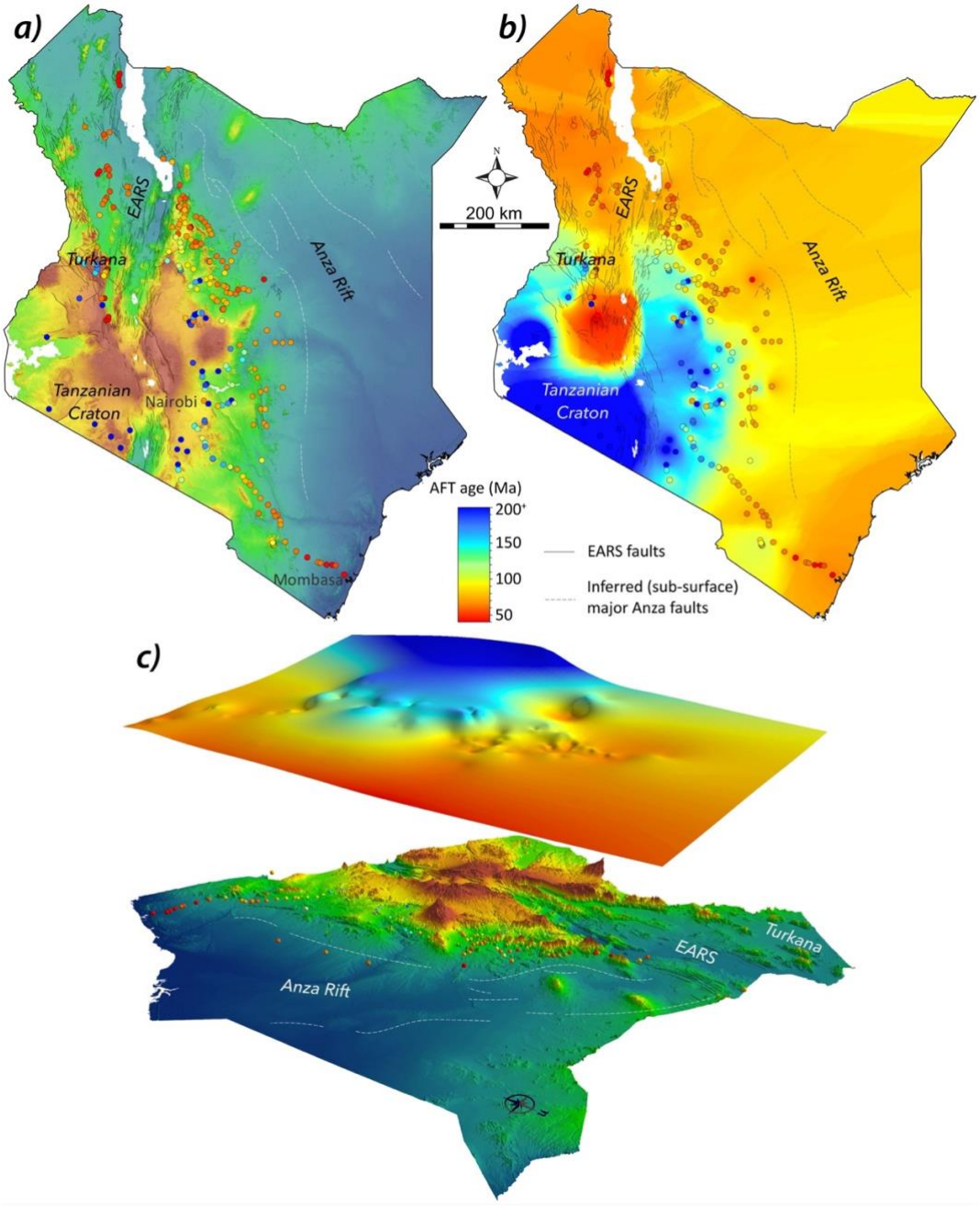

Figure 19. Decoupled trends in modern Kenyan geomorphology and AFT ages. The modern Kenyan landscape is dominated by the uplifted margins and downthrown basins of the EARS which transects the western half of the country from north to south, clearly seen in the digital elevation model (DEM) in (a) and in the vertically exaggerated DEM in (c, lower panel). Despite this, AFT ages predominantly predate the late Paleogene-recent EARS and instead mirror the distribution of the stable Archean Tanzanian Craton and Cretaceous-early Paleogene Anza Rift, as shown in the inverse distance weighted (IDW) AFT age interpolation in (b) and vertically exaggerated IDW interpolation in the upper panel of (c). The exceptions being in the Turkana region, where higher geothermal gradients and extension rates led to greater EARS-related cooling[5,41–43], and in isolated areas in the central Kenyan hydrothermal fluids thermally rejuvenated AFT ages[86].

However, despite the AARS dominating the geomorphological expression of East Africa and Arabia, the vast majority of AFT and AHe apparent ages significantly predate late Paleogene-Quaternary rifting (Figs. 19-21). This indicates that AARS-related denudation has largely been insufficient to exhume rocks from depths where geotherms exceed the temperature sensitivities of the AFT (~120-60 °C[141]) and AHe systems (~80-40 °C[164]). Only in select areas where a combination of increased net extension, lower crustal rigidity, and increased geothermal gradients are syn-rift thermochronology ages recorded, such as along the southern Red Sea margin[48], southern Gulf of Aden[80], Ethiopian Rift[28], the Turkana Depression[5,41–43] and in parts of the northern Malawi Rift[68,71]. Nevertheless, a general southward increase in AFT and AHe apparent ages is apparent (Figs. 20 & 21), mirroring an overall decrease in rift maturity and crustal heat flow.

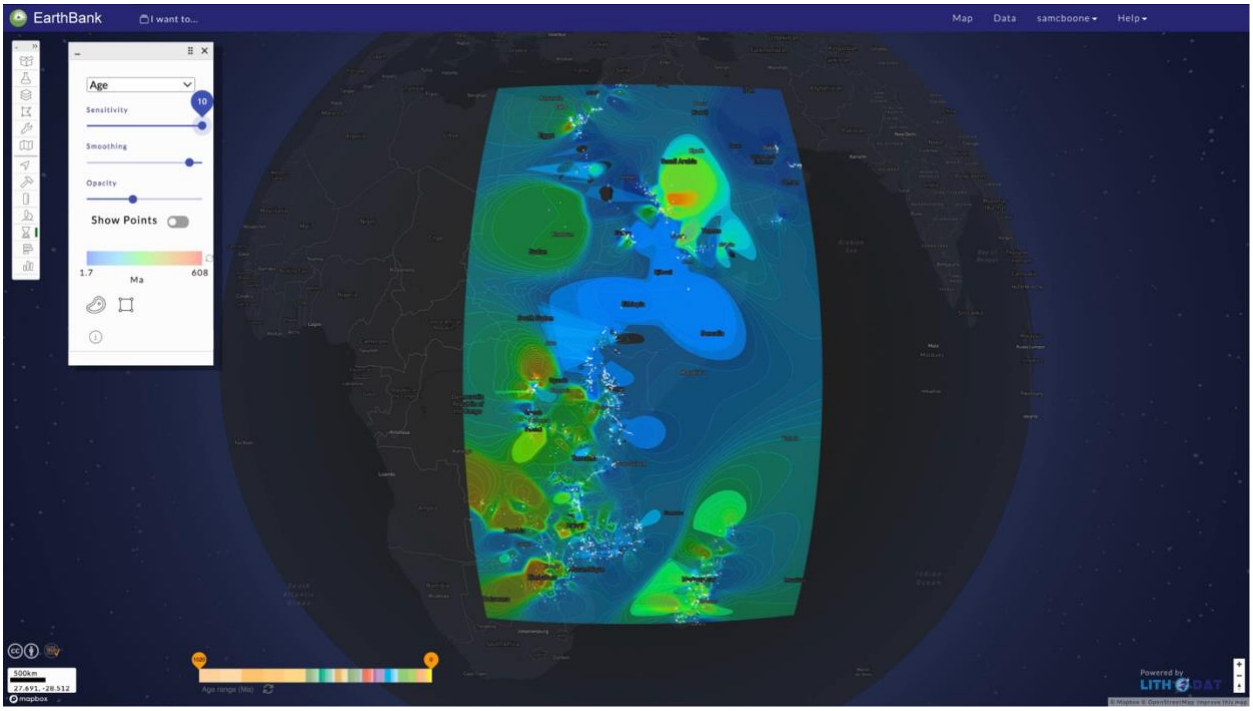

Figure 20. Spatial trends in apatite fission-track ages across the greater AARS. The inverse distance weighted data interpolation was created in EarthBank (previously AusGeochem[100,101]).

Yet, even where AFT and AHe apparent ages predate AARS rifting, they nevertheless contain valuable information about the syn-rift thermal evolution of areas in and adjacent to loci of extensional strain, which can be revealed through numerical thermal history modelling (Fig. 22). Consequently, AFT and AHe thermochronology data have been instrumental in improving our understanding of the spatiotemporal evolution of the AARS[5,93] by constraining the timing and propagation of faulting[5,62,68,71] and basin formation[28,34,41,42,48,66,77,80,83,86] throughout the region.

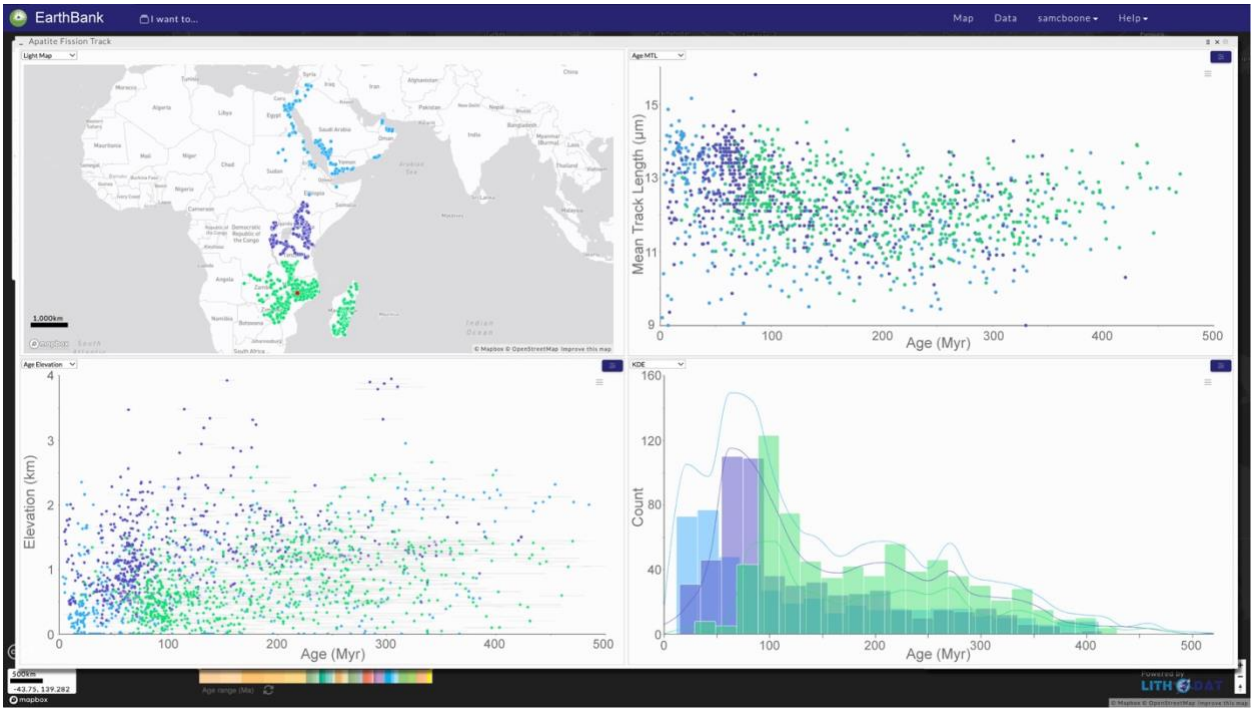

Figure 21. Apatite fission-track data trends in the AARS as shown in EarthBank (formerly AusGeochem[100,101]). Differences in apatite fission-track data trends between the northern (blue), central (purple), and southern AARS are highlighted in bivariate plots (e.g., age versus MTL, age versus elevation) and an age histogram with kernel density estimations.

Nevertheless, extrapolating periods of thermal flux recorded in time-temperature models of thermochronology data to geological causal mechanisms remains an interpretation and must therefore be done taking the local geology into careful consideration. This is because there are a wide variety of geological processes which can affect the thermal state of the upper crustal beyond just exhumation and cooling related to extensional tectonics, including in some cases changes in paleoprecipitation, basal heat flow, long-wavelength lithospheric flexure, magmatism, and hydrothermal fluid flow. Therefore, some claims that the onset of accelerated cooling in proto-rift margins reflects the initiation of basin formation due to flexural isostatic footwall uplift in response to extension[57] require further evaluation. This would include providing independent evidence for coeval syn-rift sedimentation in the associated hanging wall or a plausible explanation for non-deposition or subsequent removal of syn-rift strata. Additionally, invoked geological processes for the cause of observed crustal thermal events should be consistent with regional 3D geospatial trends in thermochronology data. Flexural isostatic footwall uplift of a basin-bounding normal fault array due to rifting, for instance, should be reflected in a diagnostic short-wavelength spatial thermochronology pattern (Fig. 23), where exhumation, and thus cooling, rapidly dissipate from maximum values immediately adjacent to the fault to background regional values in the distal footwall over a length scale that is a function of the length, angle and total displacement of that fault and lithospheric flexural rigidity[205].

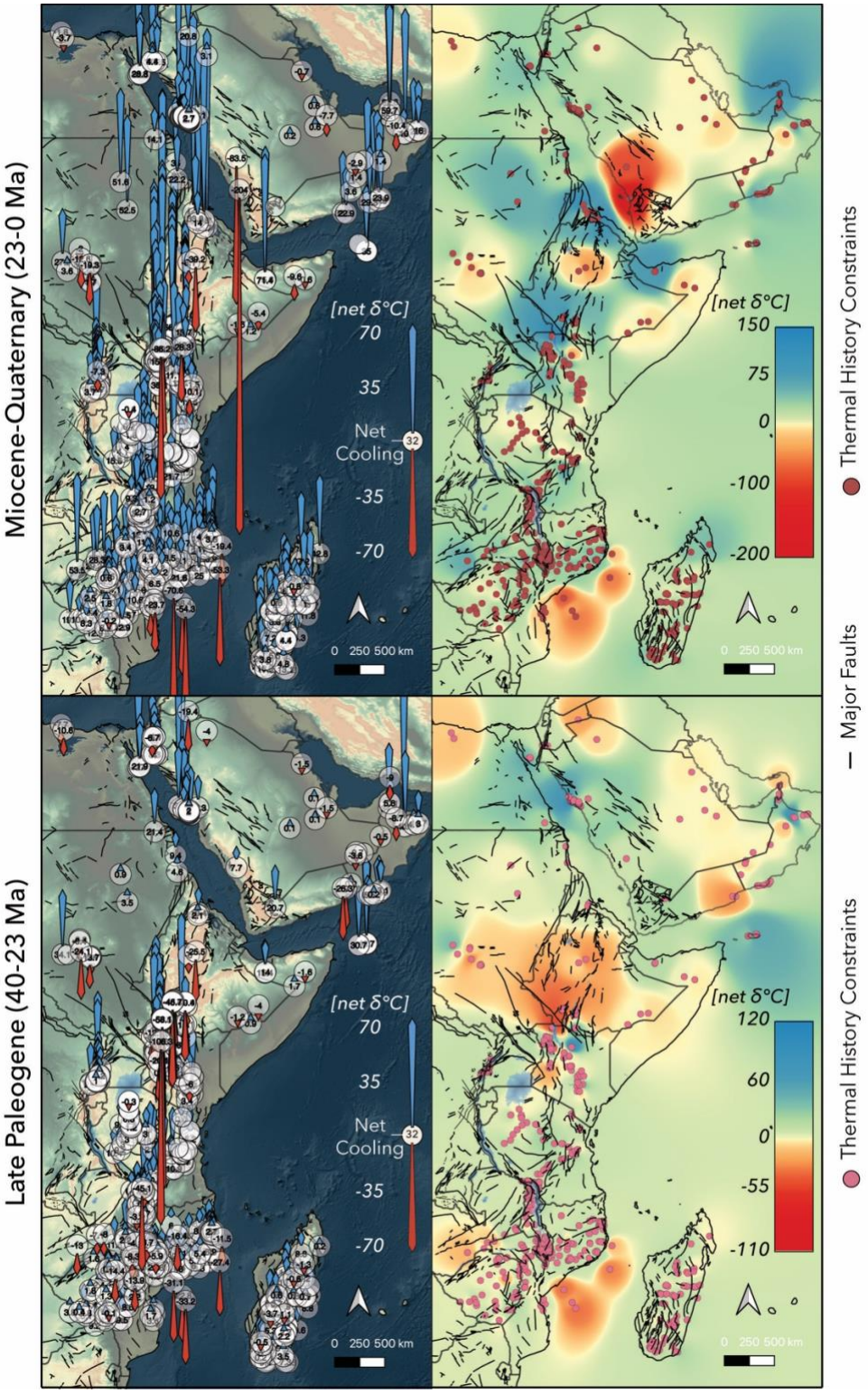

Figure 22. Regional patterns in Miocene-Quaternary (top panel) and Late Paleogene (bottom panel) upper crustal thermal histories as recorded by time-temperature models of thermochronology data and burial history models of well data. See Figure 9 for description of symbology. Note the differences in scales between the interpolations for each range in geological time.

While the sensitivity of thermochronometers to upper crustal magmatism and hydrothermal fluid is limited to the immediate country rock over the length scales of individual flow thicknesses and plutonic bodies[112,206,207], numerical models indicate that under certain conditions, these systems can be reset over a much wider area by the intrusion of large plutonic bodies in the middle crust[208]. Such broader scale thermochronology patterns should still be discernable from shorter wavelength thermal trends resulting from brittle extensional deformation. Nevertheless, consideration of these geothermal processes is critical during thermochronology interpretation, particularly when calculating denudation and burial histories from modelled cooling and heating rates. Yet to the best of the authors' knowledge, quantitative modelling of the potential effects of middle to lower crustal intrusions on Afro-Arabian Rift System thermochronology has yet to be performed.

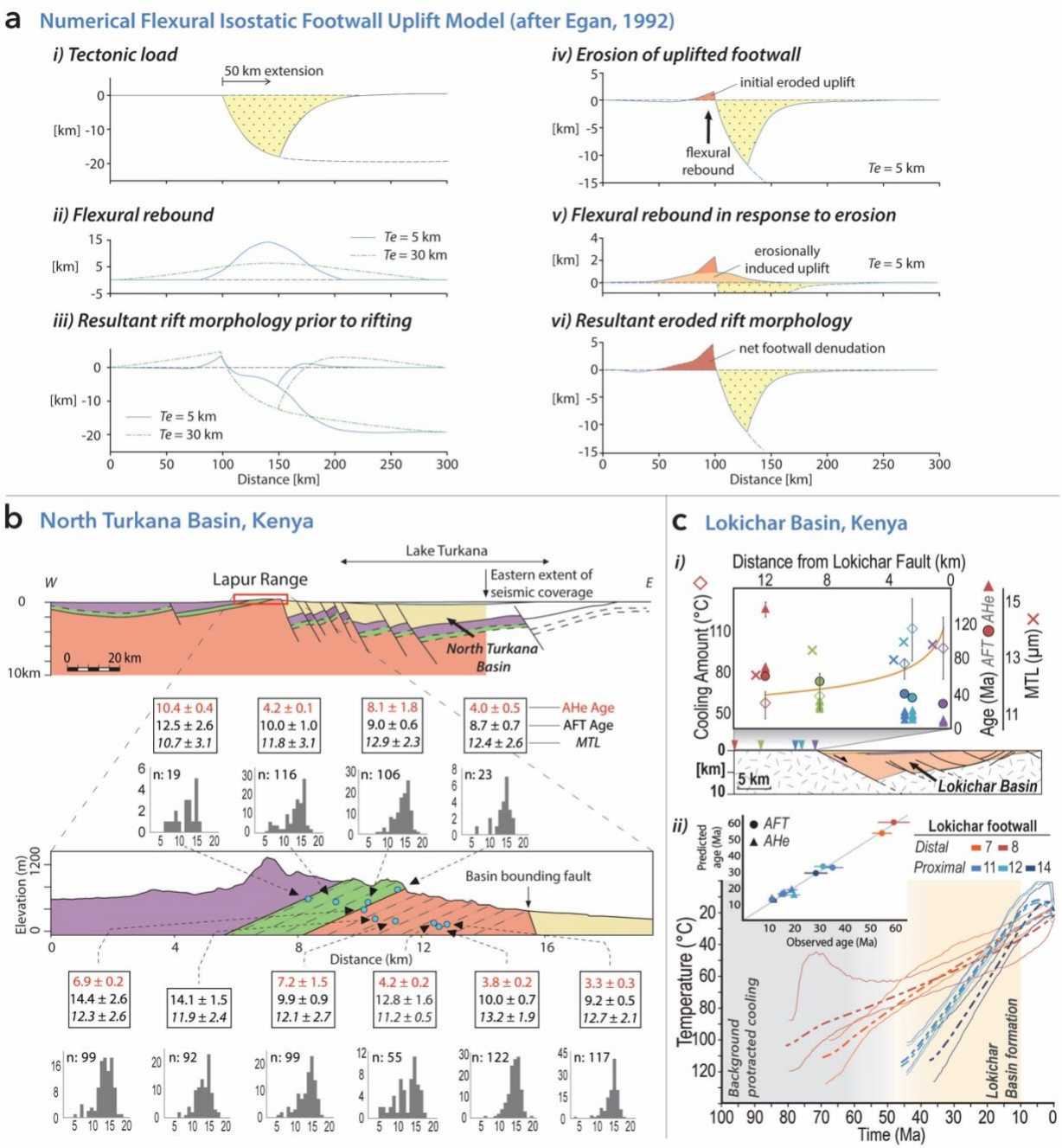

Figure 23. Spatial trends in flexural isostatic footwall uplift and thermochronology in response to extensional basin formation. (a) Numerical model of Egan[205] of flexural isostatic footwall uplift and hanging wall subsidence due to extension across a crustal-scale normal fault (a.i), illustrating the flexural response to lithospheric thinning (a.ii) and resultant rift morphology prior to erosion (a.iii), which are dependent upon lithospheric flexural rigidity (quantified here as effective elastic thickness, *Te*). After some time, the uplifted footwall erodes (a.iv), further unloading the lithosphere and inducing secondary flexural rebound (a.iv). This too is eventually eroded away to form a subdued mature rift morphology where net footwall denudation dissipates from a maximum value immediately adjacent to the basin-bounding fault to zero in the distal footwall over some tens of kilometres (a.vi). The exact width and profile of the area of denuded footwall is a product of total extension, fault geometry and lithospheric flexural rigidity. Trends in AFT and AHe

thermochronology data from exhumed basin margins reflect this, such as along (b) the North Turkana Basin[42] and (c) the Lokichar Basin[5], Kenya. As expected, apparent ages decrease and mean fission-track lengths (MTL) increase from background values in the distal footwall with increasing proximity to the basin-bounding fault systems (b & c.i). Due to the greater amount of footwall exhumation with increasing proximity to the normal fault, the onset of rapid cooling observed in thermal history models progressively approaches the timing of basin formation (c.ii). Note, the goodness of fit for Lokichar Basin thermal history models is illustrated by the observed versus predicted age plot.

Data Coverage Limitations

While the number of analyses included in this database may be large, the distribution of thermochronology data is uneven. The extent of available thermochronology data is spatially limited by surface geology and, in some cases, political boundaries. Thermochronology samples are almost exclusively limited to surface outcrops of Neoproterozoic crystalline basement and metamorphic rocks (Figs. 4 & 5) due to challenges in untangling the mixed pre- and post-depositional thermal history recorded by many Phanerozoic sedimentary rocks. Moreover, a significant portion of thermochronology studies in the region have been focused on addressing questions pertaining to the late Paleogene-recent rifting, and thus data localities are disproportionally congregated around AARS basins. Consequently, the heterogenous spread in thermochronology data across the Afro-Arabian landscape has in many cases hindered addressing questions about earlier periods of Phanerozoic tectonics or the development of long-wavelength dynamic topography[209]. Elsewhere, there remains a complete lack of low-temperature thermochronology data, including along large swathes of the Red Sea, Gulf of Aden and East African coastlines, inhibiting more holistic studies of passive margin evolution that are not focused exclusively on areas with pronounced coastal escarpments.

Future studies in the region might then consider filling some of these data gaps with the aim of achieving a more homogenously distributed thermochronology record of the Phanerozoic Afro-Arabian upper crustal thermal evolution.

Future Data Usage

The thermochronology database presented here provides powerful constraints for the 4D Phanerozoic upper crustal thermal evolution of East Africa and Arabia. However, in places significant uncertainty remains as to the accuracy and geological significance of observed periods of cooling or heating, particularly further back in deep time where data coverage is poor. These issues, in part, may stem from differences in thermal history modelling codes, methodologies and parameters used to generate the array of published time-temperature reconstructions, and by thermal history simulation non-uniqueness. To overcome these discrepancies, future studies could consider utilising the Afro-Arabian thermochronology database to bulk model all samples where

detailed single grain ages, confined track lengths and kinetic parameter data exist using a consistent modelling protocol.

Nevertheless, challenges in discerning the geological significance of specific periods of Afro-Arabian crustal thermal flux recorded by thermochronology data will remain. Disentangling these complexities will likely require future coupled geodynamic and landscape evolution modelling work that can account for 4D (3D + time) changes in crustal thermal regime due to the interplay of mantle processes, magmatism, brittle deformation, paleoclimate and surface processes.

Data Records

The low-temperature thermochronology database of the greater Afro-Arabian Rift System presented here can be freely accessed via EarthBank (previously AusGeochem[100,101]), a web-hosted, open-access geospatial data platform which enables researchers from around the world to archive, disseminate, and analyse geological, geochemical and geochronological/thermochronological data. Equipped with a range of data analysis tools, such as geosample metadata summary plots (Fig. 5), spatial data contouring (Fig. 20), bivariate, kernel density estimator and radial plotting (Figs. 13, 17 & 21), swath profile, and paleo reconstruction tools (Fig. 18), the platform enables users to geospatially interrogate thermochronology data in 4D (3D through time) in real time[101]. Users can freely register to explore and download the Afro-Arabian Rift System low-temperature thermochronology database, as well as other geosample, geochemistry, geochronology and thermochronology datasets from around the globe at https://ausgeochem.auscope.org.au. Video tutorials on how to use the platform can be found here: https://www.auscope.org.au/ausgeochem-help.

The dataset includes detailed (meta-)data for geological rock samples and their associated fission-track and (U-Th)/He data. The geological rock sample metadata is reported following the vocabulary and data structure of Boone et al.[100], including detailed location, information, sampling method, and lithological information, as well as the associated references for previously published analyses. The fission-track and (U-Th)/He data are archived in the relational database structure of Boone et al.[101], itself built on the recommendations of the Geological Society of America Bulletin special edition on "Reporting and Interpretation of Chronology Data"[102,103].

Data granularity varies drastically across the data compilation, with many legacy publications unfortunately only presenting the most basic geosample metadata and most cursory analytical data (e.g., sample location, age, and uncertainty). However, where previously published data were reported in high detail or for new fission-track data presented here, the records include detailed whole sample and single grain ages and chemistry, and confined track data on the per-track or binned (length histogram) basis. Wherever possible, including for all new analyses, (U-Th)/He data were reported in detail on a single-grain basis. Where previously published or for all new

data, calibration factors and/or associated secondary reference material results are also included in the data compilation to enable independent data quality assessment.

Technical Validation

Quality control of new thermochronological and geochemical analyses presented here was performed either via empirical calibration against primary reference materials or via the analysis of secondary reference materials of known age or composition, depending on the technique.

For apatite fission track analysis using the external detector method, an analyst-specific zeta factor was used to calibrate both the collection of difficult-to-measure variables (e.g., neutron fluxes) in the fission-track age equation and the counting behaviour of the analyst against the Durango and Fish Canyon Tuff apatite fission-track age standards (Hurford and Green, 1983). The zeta-factor for each external detector method apatite fission-track age determination is recorded in the data tables.

For laser ablation ICP-MS fission-track analyses, apatite ^{238}U determinations were validated via parallel chemical measurements of the well-characterized Durango apatite (12.2 ± 0.1 ppm) and an in-house sintered Mud Tank carbonatite apatite (3.00 ± 0.01 ppm) as secondary reference materials, following the procedure of Seiler et al.[155].

Prior to the EPMA of unknowns, JEOL JXA-8530F FEG electron probe microanalyser was tuned using a series of in-house standards of known composition for each element measured (F, P, Cl, Ca, Sr, Na, Ce, La, Mn, Mg, Fe, K, Y, S, and Si). The quality of each spot analysis was then assessed by their corresponding total count, with analyses yielding a count of 99-100.5 considered acceptable.

(U-Th)/He data quality was assessed via the analysis of secondary reference materials of known ages, the results of which are included in the data reports. For zircon (U-Th)/He, each analytical batch included multiple aliquots of Fish Canyon zircon (28.4 ± 0.2 Ma)[169], while Durango apatite (31.02 ± 1.01 Ma)[210] was run as a secondary reference material during apatite (U-Th-Sm)/He analysis. (U-Th)/He analyses of secondary reference materials consistently produced ages within error of the accepted values, yielding mean ages (reported at 2σ) for the Fish Canyon Tuff zircon of 28.6 ± 2.2 Ma (n= 9) and the Durango apatite of 31.1 ± 1.6 Ma (n= 25).

Usage Notes

The AARS thermochronology database is available for download from the EarthBank data platform[100,101], itself licensed under a Creative Commons Attribution 4.0 International License

(DOI: 10.58024/AGUM97FC4439). Acknowledgement of the data repository, this manuscript and the original sources of any relevant legacy data included within the database is requested.

Acknowledgements

The Melbourne Thermochronology Research Group has received significant support over several years from the AuScope program (www.auscope.org.au) of the Australian National Collaborative Research Infrastructure Strategy (NCRIS), the Australian Research Council and Australian Geodynamics Cooperative Research Centre for the procurement of analytical instrumentation and production of thermochronology data. SB received research funding from a University of Melbourne Early Career Researcher Grant.

Author contributions

S.B. conceived of the project, led data collation and synthesis, conducted fieldwork sampling in Kenya and Malawi, produced new fission track and (U-Th)/He data in Kenya, Ethiopia and Malawi, generated many of the figures and wrote the manuscript.

M.M performed data collation and synthesis, conducted fieldwork sampling in Malawi, produced new fission track and (U-Th)/He data in Kenya and Malawi, generated many of the figures and provided feedback during manuscript preparation.

M-L.B. performed data collation and synthesis, conducted fieldwork sampling in Ethiopia, provided previously unpublished fission track data from Ethiopia, and provided feedback during manuscript preparation.

B.K. conducted fieldwork sampling in Kenya, produced new (U-Th)/He data in Kenya, Ethiopia, Malawi and Zimbabwe, and provided feedback during manuscript preparation.

A.G. conducted fieldwork sampling in Kenya, provided previously unpublished fission track data from Kenya, and provided feedback during manuscript preparation.

A.A. produced new (U-Th)/He data in Kenya, Ethiopia, Malawi and Zimbabwe.

G.H. performed electron probe microanalysis.

W.N. conducted fieldwork sampling in Kenya, Tanzania, Malawi and Zimbabwe, provided previously unpublished fission track data from Kenya and Tanzania.

V.M. produced new fission track and (U-Th)/He data from Zimbabwe.

C.S. performed field work and sample collection in Kenya.

D.B. conducted fieldwork sampling in Kenya, Tanzania, Malawi and Zimbabwe, provided previously unpublished fission track data from Zimbabwe, and provided feedback during manuscript preparation.

D.M-K. produced new fission track data from Kenya, and provided feedback during manuscript preparation.

D.S. provided detailed zircon and apatite (U-Th)/He data from Egypt.

J.J. provided detailed fission track and (U-Th)/He data from Mozambique, and provided feedback during manuscript preparation.

E.P. provided detailed zircon and apatite (U-Th)/He data from Egypt.

M.D. provided previously unpublished fission track and (U-Th)/He data from Mozambique, and provided feedback during manuscript preparation.

F.K. performed data collation and synthesis, and provided feedback during manuscript preparation.

R.B. performed data collation and synthesis, and provided feedback during manuscript preparation.

Competing interests

The authors declare that there are no competing interests.

References

1. Catuneanu, O. *et al.* The Karoo basins of south-central Africa. *J. African Earth Sci.* **43**, 211–253 (2005).
2. Thompson, J. O., Moulin, M., Aslanian, D., de Clarens, P. & Guillocheau, F. New starting point for the Indian Ocean: Second phase of breakup for Gondwana. *Earth-Science Rev.* **191**, 26–56 (2019).
3. Davison, I. & Steel, I. Geology and hydrocarbon potential of the East African continental margin : a review. *Pet. Geosci.* (2017).
4. Macgregor, D. History of the development of Permian-Cretaceous rifts in East Africa: a series of interpreted maps through time. *Pet. Geosci.* (2017).
5. Boone, S. C. *et al.* Birth of the East African Rift System: Nucleation of magmatism and strain in the Turkana Depression. *Geology* **47**, 886–890 (2019).
6. Morley, C. K., Stone, D. M., Harper, R. M. & Wigger, S. T. Geology and Geophysics of the Western Turkana Basins , Kenya. in *Geoscience of Rift Systems—Evolution of East Africa: AAPG Studies in Geology No. 44* (ed. Morley, C. K.) 19–54 (1999).
7. Ebinger, C. J. & Sleep, N. H. Cenozoic magnatism throughout east Africa resulting from impact of a single plume. *Nature* **395**, 788–791 (1998).
8. Rooney, T. O. The Cenozoic magmatism of East-Africa: Part I — Flood basalts and pulsed magmatism. *Lithos* **286**–**287**, 264–301 (2017).
9. Wolfenden, E., Ebinger, C., Yirgu, G., Renne, P. R. & Kelley, S. P. Evolution of a volcanic rifted margin: Southern Red Sea, Ethiopia. *Bull. Geol. Soc. Am.* **117**, 846–864 (2005).

10. Ayalew, D. *et al.* Temporal compositional variation of syn-rift rhyolites along the western margin of the southern Red Sea and northern Main Ethiopian Rift. *Geol. Soc. Spec. Publ.* **259**, 121–130 (2006).
11. Roberts, E. M. *et al.* Initiation of the western branch of the East African Rift coeval with the eastern branch. *Nat. Geosci.* **5**, 289–294 (2012).
12. Morley, C. K., Ngenoh, D. K. & Ego, J. K. Introduction to the East African Rift System. in *Geoscience of Rift Systems-Evolution of East Africa: AAPG Studies in Geology No. 44* (ed. Morley, C. K.) 1–18 (1999).
13. Stamps, D. S., Kreemer, C., Fernandes, R., Rajaonarison, T. A. & Rambolamanana, G. Redefining East African Rift System kinematics. *Geology* **49**, 150–155 (2021).
14. Augustin, N., van der Zwan, F. M., Devey, C. W. & Brandsdóttir, B. 13 million years of seafloor spreading throughout the Red Sea Basin. *Nat. Commun.* **12**, (2021).
15. Fournier, M. *et al.* Arabia-Somalia plate kinematics, evolution of the Aden-OwenCarlsberg triple junction, and opening of the Gulf of Aden. *J. Geophys. Res. Solid Earth* **115**, 1–24 (2010).
16. Grant, C., Kolawole, F. & Williams, J. Evolution of rift faulting in incipient, magma-poor divergent plate boundaries: New insights from the Okavango-Makgadikgadi Rift Zone, Botswana. *Earth Planet. Sci. Lett.* **646**, 118957 (2024).
17. Sippel, J. *et al.* The Kenya rift revisited: insights into lithospheric strength through data-driven 3-D gravity and thermal modelling. *Solid Earth* **8**, 45–81 (2017).
18. Adams, A., Miller, J. & Accardo, N. Relationships Between Lithospheric Structures and Rifting in the East African Rift System: A Rayleigh Wave Tomography Study. *Geochemistry, Geophys. Geosystems* **19**, 3793–3810 (2018).
19. Daly, E. *et al.* Crustal tomographic imaging of a transitional continental rift: The Ethiopian rift. *Geophys. J. Int.* **172**, 1033–1048 (2008).
20. Rooney, T. The Cenozoic magmatism of East Africa: Part II–Rifting of the mobile belt. *Lithos* **360**, (2020).
21. Rooney, T. O. The Cenozoic magmatism of East Africa: Part V – Magma sources and processes in the East African Rift. *Lithos* **360**–**361**, 105296 (2020).
22. McDougall, I. & Brown, F. H. Timing of volcanism and evolution of the northern Kenya Rift. *Geol. Mag.* **146**, 34–47 (2009).
23. Fritz, H. *et al.* Orogen styles in the East African Orogen: A review of the Neoproterozoic to Cambrian tectonic evolution. *J. African Earth Sci.* **86**, 65–106 (2013).
24. Collins, A. S., Blades, M. L., Merdith, A. S. & Foden, J. D. Closure of the Proterozoic Mozambique Ocean was instigated by a late Tonian plate reorganization event. *Nat. Commun. Earth Environ.* **2**, 1–7 (2021).
25. Boger, S. D. *et al.* The 580-520Ma Gondwana suture of Madagascar and its continuation into Antarctica and Africa. *Gondwana Res.* **28**, 1048–1060 (2015).
26. Purcell, P. G. Re-imagining and re-imaging the development of the East African Rift. *Pet. Geosci.* **36**, (2017).
27. Thiéblemont, D. *et al.* Geological Map of Africa at 1:10M scale. (2016).
28. Abebe, T., Balestrieri, M. L. & Bigazzi, G. The Central Main Ethiopian Rift is younger than 8 Ma: confirmation through apatite fission-track thermochronology. *Terra Nov.* **22**, 470–476 (2010).
29. Abbate, E., Balestrieri, M. L. & Bigazzi, G. Uplifted rift-shoulder of the Gulf of Aden in northwestern Somalia: Palinspastic reconstructions supported by apatite fission-track data. *Mémoires du Muséum Natl. d'histoire Nat.* **186**, 629–640 (2001).
30. Abbate, E., Balestrieri, M. L. & Bigazzi, G. Morphostructural development of the Eritrean rift flank (southern Red Sea) inferred from apatite fission track analysis. *J. Geophys. Res.* **107**, 1–12 (2002).
31. Alessio, B. L. *et al.* The thermo-tectonic evolution of the southern Congo Craton margin as determined from apatite and muscovite thermochronology. *Tectonophysics* **766**, 398–415 (2019).
32. Balestrieri, M. L., Stuart, F. M., Persano, C., Abbate, E. & Bigazzi, G. Geomorphic development of the escarpment of the Eritrean margin, southern Red Sea from combined apatite fission-track and

(U-Th)/He thermochronometry. *Earth Planet. Sci. Lett.* **231**, 97–110 (2005).
33. Balestrieri, M. L., Abbate, E., Bigazzi, G. & Ali, O. E. B. Thermochronological data from Sudan in the frame of the denudational history of the Nubian Red Sea margin. *Earth Surf. Process. Landforms* **34**, 1279–1290 (2009).
34. Balestrieri, M. L., Bonini, M., Corti, G., Sani, F. & Philippon, M. A refinement of the chronology of rift-related faulting in the Broadly Rifted Zone, southern Ethiopia, through apatite fission-track analysis. *Tectonophysics* **671**, 42–55 (2016).
35. Bauer, F. U. *et al.* Tracing the exhumation history of the Rwenzori Mountains, Albertine Rift, Uganda, using low-temperature thermochronology. *Tectonophysics* **599**, 8–28 (2013).
36. Bauer, F. U. *et al.* Long-term cooling history of the Albertine Rift: new evidence from the western rift shoulder, D.R. Congo. *Int. J. Earth Sci.* **105**, 1707–1728 (2016).
37. Bicca, M. M., Jelinek, A. R., Philipp, R. P. & Jamal, D. L. Mesozoic-Cenozoic landscape evolution of NW Mozambique recorded by apatite thermochronology. *J. Geodyn.* **125**, 48–65 (2019).
38. Belton, D. X. & Raab, M. J. Cretaceous reactivation and intensified erosion in the Archean-Proterozoic Limpopo Belt, demonstrated by apatite fission track thermochronology. *Tectonophysics* **480**, 99–108 (2010).
39. Bohannon, R. G., Naeser, C. W., Schmidt, D. L. & Zimmermann, R. A. The timing of uplift, volcanism, and rifting peripheral to the Red Sea: A case for passive rifting? *J. Geophys. Res.* **94**, 1683–1701 (1989).
40. Bojar, A.-V., Fritz, H., Kargl, S. & Unzog, W. Phanerozoic tectonothermal history of the Arabian–Nubian shield in the Eastern Desert of Egypt: evidence from fission track and paleostress data. *J. African Earth Sci.* **34**, 191–202 (2002).
41. Boone, S. C. *et al.* Tectono-thermal evolution of a long-lived segment of the East African Rift System: Thermochronological insights from the North Lokichar Basin, Turkana, Kenya. *Tectonophysics* **744**, 23–46 (2018).
42. Boone, S. C. *et al.* Influence of Rift Superposition on Lithospheric Response to East African Rift System Extension: Lapur Range, Turkana, Kenya. *Tectonics* **37**, 1–26 (2018).
43. Boone, S. C. *et al.* Tectonothermal Evolution of the Broadly Rifted Zone, Ethiopian Rift. *Tectonics* **38**, 1070–1100 (2019).
44. Daszinnies, M. C., Jacobs, J., Wartho, J. A. & Grantham, G. H. Post pan-african thermo-tectonic evolution of the north Mozambican basement and its implication for the Gondwana rifting. Inferences from 40Ar/ 39Ar hornblende, biotite and titanite fission-track dating. *Geol. Soc. Spec. Publ.* **324**, 261–286 (2009).
45. Emmel, B. *et al.* The low-temperature thermochronological record of sedimentary rocks from the central Rovuma Basin (N Mozambique) - Constraints on provenance and thermal history. *Gondwana Res.* **25**, 1216–1229 (2014).
46. Emmel, B. *et al.* From closure of the Mozambique Ocean to gondwana breakup: New evidence from geochronological data of the Vohibory terrane, Southwest Madagascar. *J. Geol.* **116**, 21–38 (2008).
47. Feinstein, S. *et al.* Uplift and denudation history of the eastern Dead Sea rift fl ank , SW Jordan : Evidence from apatite fi ssion track thermochronometry. *Tectonics* **32**, 1513–1528 (2013).
48. Ghebreab, W., Carter, A., Hurford, A. J. & Jouniaux, L. Constraints for timing of extensional tectonics in the western margin of the Red Sea in Eritrea. *Earth Planet. Sci. Lett.* **200**, 107–119 (2002).
49. Foster, D. A. & Gleadow, A. J. W. The morphotectonic evolution of rift-margin mountains in central Kenya: Constraints from apatite fission-track thermochronology. *Earth Planet. Sci. Lett.* **113**, 157–171 (1992).
50. Foster, D. A. & Gleadow, J. W. Structural framework and denudation history of the flanks of the Kenya and Anza Rifts , East Africa. *Tectonics* **15**, 258–271 (1996).
51. Gleadow, A. J. W. Fission track age of the KBS Tuff and associated hominid remains in northern Kenya. *Nature* **284**, 225–230 (1980).
52. Fernandes, P. *et al.* The thermal history of the Karoo Moatize-Minjova Basin, Tete Province,

Mozambique: An integrated vitrinite reflectance and apatite fission track thermochronology study. *J. African Earth Sci.* **112**, 55–72 (2015).
53. Eby, G. N. *et al.* Geochronology and cooling history of the northern part of the Chilwa Alkaline Province, Malawi. *J. African Earth Sci.* **20**, 275–288 (1995).
54. Gunnell, Y., Carter, A., Petit, C. & Fournier, M. Post-rift seaward downwarping at passive margins: New insights from southern Oman using stratigraphy to constrain apatite fission-track and (U-Th)/He dating. *Geology* **35**, 647–650 (2007).
55. Hansman, R. J., Ring, U., Thomson, S. N., den Brok, B. & Stübner, K. Late Eocene Uplift of the Al Hajar Mountains, Oman, Supported by Stratigraphy and Low-Temperature Thermochronology. *Tectonics* **36**, 3081–3109 (2017).
56. Jacobs, J., Thomas, R. J., Ksienzyk, A. K. & Dunkl, I. Tracking the Oman Ophiolite to the surface - New fission track and (U-Th)/He data from the Aswad and Khor Fakkan Blocks, United Arab Emirates. *Tectonophysics* **644**, 68–80 (2015).
57. Jess, S. *et al.* Paleogene initiation of the Western Branch of the East African Rift: The uplift history of the Rwenzori Mountains, Western Uganda. *Earth Planet. Sci. Lett.* **552**, 116593 (2020).
58. Kasanzu, C. H. Apatite fission track and (U-Th)/He thermochronology from the Archean Tanzania craton: Contributions to cooling histories of Tanzanian basement rocks. *Geosci. Front.* 1–9 (2016) doi:10.1016/j.gsf.2016.09.007.
59. Kasanzu, C. H. *et al.* From source to sink in central Gondwana: Exhumation of the Precambrian basement rocks of Tanzania and sediment accumulation in the adjacent Congo basin. *Tectonics* **35**, 2034–2051 (2016).
60. Kohn, B. P. & Eyal, E. History of uplift of the crystalline basement of Sinai and its relation to opening of the Red Sea as revealed by fission track dating of apatites. *Earth Planet. Sci. Lett.* **52**, 129–141 (1981).
61. Kohn, B. P., Feinstein, S., Foster, D. A., Steckler, M. S. & Eyal, M. Thermal history of the eastern Gulf of Suez, II. Reconstruction from apatite fission track and 40Ar/39Ar K-feldspar measurements. *Tectonophysics* **283**, 219–239 (1997).
62. Kohn, B., Weissbrod, T., Chung, L., Farley, K. & Bodorkos, S. Low-temperature thermochronology of francolite: Insights into timing of Dead Sea Transform motion. *Terra Nov.* **31**, 205–219 (2019).
63. Mackintosh, V., Kohn, B., Gleadow, A. & Tian, Y. Phanerozoic Morphotectonic Evolution of the Zimbabwe Craton: Unexpected Outcomes From a Multiple Low-Temperature Thermochronology Study. *Tectonics* **36**, 2044–2067 (2017).
64. Mackintosh, V., Kohn, B., Gleadow, A. & Gallagher, K. Long-term reactivation and morphotectonic history of the Zambezi Belt, northern Zimbabwe, revealed by multi-method thermochronometry. *Tectonophysics* **750**, 117–136 (2019).
65. Mackintosh, V., Kohn, B., Gleadow, A. & Belton, D. X. Thermochronological insights into the morphotectonic evolution of the Eastern Highlands, Zimbabwe: Implications for thermal history modelling of multi-thermochronometer data. *J. African Earth Sci.* **158**, 103542 (2019).
66. van der Beek, P., Mbede, E., Andriessen, P. & Delvaux, D. Denudation history of the Malawi and Rukwa Rift flanks (East African Rift system) from apatite fission track thermochronology. *J. African Earth Sci.* **26**, 363–385 (1998).
67. McMillan, M. F., Boone, S. C., Kohn, B. P., Gleadow, A. J. & Chindandali, P. R. Development of the Nyika Plateau, Malawi: A Long Lived Paleo-Surface or a Contemporary Feature of the East African Rift? *Geochemistry, Geophys. Geosystems* **23**, (2022).
68. McMillan, M., Boone, S. C., Chindandali, P., Kohn, B. & Gleadow, A. 4D fault evolution revealed by footwall exhumation modelling: A natural experiment in the Malawi Rift. *J. Struct. Geol.* **187**, 105196 (2024).
69. Menzies, M., Gallagher, K., Yelland, A. & Hurford, A. J. Volcanic and nonvolcanic rifted margins of the Red Sea and Gulf of Aden: Crustal cooling and margin evolution in Yemen. *Geochemica Cosmochim. Acta* **61**, 2511–2527 (1997).
70. Morag, N., Haviv, I., Eyal, M., Kohn, B. P. & Feinstein, S. Early flank uplift along the Suez Rift:

Implications for the role of mantle plumes and the onset of the Dead Sea Transform. *Earth Planet. Sci. Lett.* **516**, 56–65 (2019).
71. Mortimer, E., Kirstein, L. A., Stuart, F. M. & Strecker, M. R. Spatio-temporal trends in normal-fault segmentation recorded by low-temperature thermochronology: Livingstone fault scarp, Malawi Rift, East African Rift System. *Earth Planet. Sci. Lett.* **455**, 62–72 (2016).
72. Mount, V. S., Crawford, R. I. S. & Bergman, S. C. Regional structural style of the Central and Southern Oman Mountains: Jebel Akhdar, Saih Hatat, and the Northern Ghaba Basin. *GeoArabia* **3**, 475–490 (1998).
73. Naylor, D., Al-Rawi, M., Clayton, G., Fitzpatrick, M. J. & Green, P. F. Hydrocarbon potential in Jordan. *J. Pet. Geol.* **36**, 205–236 (2013).
74. Noble, W. P., Foster, D. A. & Gleadow, A. J. W. The post-Pan-African thermal and extensional history of crystalline basement rocks in eastern Tanzania. *Tectonophysics* **275**, 331–350 (1997).
75. Omar, G. I., Kohn, B. P., Lutz, T. M. & Faul, H. The cooling history of Silurian to Cretaceous alkaline ring complexes, south Eastern Desert, Egypt, as revealed by fission-track analysis. *Earth Planet. Sci. Lett.* **83**, 94–108 (1987).
76. Omar, G. I., Steckler, M. S., Buck, W. R. & Kohn, B. P. Fission-track analysis of basement apatites at the western margin of the Gulf of Suez rift, Egypt: evidence for synchroneity of uplift and subsidence. *Earth Planet. Sci. Lett.* **94**, 316–328 (1989).
77. Philippon, M. *et al.* Evolution, distribution, and characteristics of rifting in southern Ethiopia. *Tectonics* **33**, 485–508 (2014).
78. Pik, R., Marty, B., Carignan, J. & Lavé, J. Stability of the Upper Nile drainage network (Ethiopia) deduced from (U-Th)/He thermochronometry: implications for uplift and erosion of the Afar plume dome. *Earth P* **215**, 73–88 (2003).
79. Pik, R., Marty, B., Carignan, J., Yirgu, G. & Ayalew, T. Timing of East African Rift development in southern Ethiopia : Implication for mantle plume activity and evolution of topography. *Geology* **36**, 167–170 (2008).
80. Pik, R. *et al.* Structural control of basement denudation during rifting revealed by low-temperature (U-Th-Sm)/He thermochronology of the Socotra Island basement-Southern Gulf of Aden margin. *Tectonophysics* **607**, 17–31 (2013).
81. Poupeau, G., Saddiqi, O., Michard, A., Goffé, B. & Oberhänsli, R. Late thermal evolution of the Oman Mountains subophiolitic windows apatite fission-track thermochronology. *Geology* **26**, 1139–1142 (1998).
82. Saddiqi, O., Michard, A., Goffe, B., Poupeau, G. & Oberhänsli, R. Fission-track thermochronology of the Oman Mountains continental windows, and current problems of tectonic interpretation. *Bull. la Soc. Geol. Fr.* **177**, 127–143 (2006).
83. Spiegel, C., Kohn, B. P., Belton, D. X. & Gleadow, A. J. W. Morphotectonic evolution of the central Kenya rift flanks: Implications for late Cenozoic environmental change in East Africa. *Geology* **35**, 427–430 (2007).
84. Szymanski, E., Stockli, D. F., Johnson, P. R. & Hager, C. Thermochronometric evidence for diffuse extension and two-phase rifting within the Central Arabian Margin of the Red Sea Rift. *Tectonics* **35**, 2863–2895 (2016).
85. Tarapoanca, M. *et al.* Forward kinematic modelling of a regional transect in the Northern Emirates using geological and apatite fission track age constraints on paleo-burial history-. *Arab. J. Geosci.* **3**, 395–411 (2010).
86. Torres Acosta, V. *et al.* Cenozoic extension in the Kenya Rift from low-temperature thermochronology: Links to diachronous spatiotemporal evolution of rifting in East Africa. *Tectonics* **34**, 2367–2386 (2015).
87. Ojo, O., Thomson, S. N. & Laó-Dávila, D. A. Neogene–Quaternary initiation of the Southern Malawi Rift and linkage to the reactivated Carboniferous–Jurassic Shire Rift. *Tectonophysics* **877**, (2024).
88. van den Haute, P. Fission-track ages of apatites from the Precambrian of Rwanda and Burundi:

relationship to East African rift tectonics. *Earth Planet. Sci. Lett.* **71**, 129–140 (1984).
89. Vermeesch, P., Avigad, D. & McWilliams, M. O. 500 m.y. of thermal history elucidated by multi-method detrital thermochronology of North Gondwana Cambrian sandstone (Eilat area, Israel). *Bull. Geol. Soc. Am.* **121**, 1204–1216 (2009).
90. Wagner, M., Altherr, R. & Van Den Haute, P. Apatite fission-track analysis of Kenyan basement rocks: constraints on the thermotectonic evolution of the Kenya dome. A reconnaissance study. *Tectonophysics* **204**, 93–110 (1992).
91. Daßinnies, M. The Phanerozoic thermo-tectonic evolution of northern Mozambique constrained by 40Ar-39Ar, fission track and (U-Th)-He analyses. (University of Bremen, 2006).
92. Boone, S. C., Balestrieri, M. L. & Kohn, B. Tectono-Thermal Evolution of the Red Sea Rift. *Front. Earth Sci.* **9**, 1–9 (2021).
93. Boone, S. C., Balestrieri, M. L. & Kohn, B. Thermo-tectonic imaging of the Gulf of Aden-Red Sea rift systems and Afro-Arabian hinterland. *Earth-Science Rev.* **222**, (2021).
94. Boone, S. C. *et al.* Tectonothermal Evolution of the Broadly Rifted Zone, Ethiopian Rift. *Tectonics* **38**, (2019).
95. Zawacki, E. E. *et al.* Sediment provenance and silicic volcano-tectonic evolution of the northern East African Rift System from U/Pb and (U-Th)/He laser ablation double dating of detrital zircons. *Earth Planet. Sci. Lett.* **580**, 117375 (2022).
96. Veeningen, R., Rice, A. H. N., Schneider, D. A. & Grasemann, B. Thermochronology and geochemistry of the Pan-African basement below the Sab'atayn Basin, Yemen. *J. African Earth Sci.* **102**, 131–148 (2015).
97. Emmel, B. *et al.* Thermochronological history of an orogen-passive margin system: An example from northern Mozambique. *Tectonics* **30**, (2011).
98. Boone, S. C., Balestrieri, M. L. & Kohn, B. Thermo-tectonic imaging of the Gulf of Aden-Red Sea rift systems and Afro-Arabian hinterland. *Earth-Science Rev.* **222**, 103824 (2021).
99. Stockli, D. F. & Bosworth, W. Timing of extensional faulting along the magma-poor central and northern Red Sea rift margin—transition from regional extension to necking along a hyperextended rifted margin. in *Geological setting, palaeoenvironment and archaeology of the Red Sea* 81–111 (Springer, 2018).
100. Boone, S. C. *et al.* AusGeochem: An Open Platform for Geochemical Data Preservation, Dissemination and Synthesis. *Geostand. Geoanalytical Res.* (2022) doi:10.1111/ggr.12419.
101. Boone, S. C. *et al.* A geospatial platform for the tectonic interpretation of low-temperature thermochronology Big Data. *Sci. Rep.* **13**, 1–15 (2023).
102. Kohn, B. P. *et al.* Interpreting and reporting fission-track chronological data. *Geol. Soc. Am. Bull.* 1–30 (2024) doi:10.1130/b37245.1.
103. Flowers, R. M. *et al.* (U-Th)/He chronology: Part 1. Data, uncertainty, and reporting. *GSA Bull.* **135**, 104–136 (2023).
104. Gallagher, K. Transdimensional inverse thermal history modeling for quantitative thermochronology. *J. Geophys. Res. Solid Earth* **117**, 1–16 (2012).
105. Ketcham, R. A. Forward and inverse modeling of low-temperature thermochronometry data. *Rev. Mineral. Geochemistry* **58**, 275–314 (2005).
106. Ketcham, R. A., Carter, A., Donelick, R. A., Barbarand, J. & Hurford, A. J. Improved modeling of fission-track annealing in apatite. *Am. Mineral.* **92**, 799–810 (2007).
107. Flowers, R. M., Ketcham, R. A., Shuster, D. L. & Farley, K. A. Apatite (U-Th)/He thermochronometry using a radiation damage accumulation and annealing model. *Geochim. Cosmochim. Acta* **73**, 2347–2365 (2009).
108. Guenthner, W. R., Reiners, P. W., Ketcham, R. A., Nasdala, L. & Giester, G. Helium diffusion in natural zircon: radiation damage, anisotropy, and the interpretation of zircon (U-TH)/He thermochronology. *Am. J. Sci.* **313**, 145–198 (2013).
109. Gautheron, C., Tassan-Got, L., Barbarand, J. & Pagel, M. Effect of alpha-damage annealing on apatite (U-Th)/He thermochronology. *Chem. Geol.* **266**, 157–170 (2009).

110. Ginster, U., Reiners, P. W., Nasdala, L. & Chanmuang N., C. Annealing kinetics of radiation damage in zircon. *Geochim. Cosmochim. Acta* **249**, 225–246 (2019).
111. Stockli, D. F. Application of Low-Temperature Thermochronometry to Extensional Tectonic Settings. *Rev. Mineral. Geochemistry* **58**, 411–448 (2005).
112. Ehlers, T. A. Crustal thermal processes and the interpretation of thermochronometer data. *Rev. Mineral. Geochemistry* **58**, 315–350 (2005).
113. Foster, D. A. Fission-Track Thermochronology in Structural Geology and Tectonic Studies. in *Fission-Track Thermochronology and its Application to Geology* 211–220 (Springer International Publishing, 2019). doi:10.1007/978-3-319-89421-8_11.
114. Mohamed, A. Y., Iliffe, J. E., Ashcroft, W. A. & Whiteman, A. J. Burial and maturation history of the Heglig field area, Muglad Basin, Sudan. *J. Pet. Geol.* **23**, 107–128 (2000).
115. Mohamed, A. Y., Pearson, M. J., Ashcroft, W. A. & Whiteman, A. J. Petroleum maturation modelling, Abu Gabra-Sharaf area, Muglad Basin, Sudan. *J. African Earth Sci.* **35**, 331–344 (2002).
116. Gebbayin, O. I. M. F. A., Zhong, N., Ibrahim, G. A. & Alzain, M. A. Origin of a Tertiary oil from El Mahafir wildcat & geochemical correlation to some Muglad source rocks, Muglad basin, Sudan. *J. African Earth Sci.* **137**, 133–148 (2018).
117. Terken, J. M. J. The Natih petroleum system of north Oman. *GeoArabia* **4**, 157–180 (1999).
118. Shalaby, M. R., Abdullah, W. H. & Abu Shady, A. N. Burial history, basin modeling and petroleum source potential in the Western Desert, Egypt. *Bull. Geol. Soc. Malaysia* **54**, 103–113 (2008).
119. Tsegaye, S. G., Nton, M. E., Boboye, O. A. & Ahmed, W. Geochemical Characteristics and Hydrocarbon Generation Modelling of Early Triassic to Late Cretaceous Formations within Ogaden Basin, Ethiopia. *J. Pet. Sci. Technol.* **8**, 58–75 (2018).
120. Ayodele, I. J., Orimolade, A., Adetola, S., Penfield G. & Falaye, B. High impact exploration inventory in an emerging hydrocarbon province, Morondava Basin, Offshore Madagascar. in *AAPG 2017 Annual Convention and Exhibition, Houston, Texas* 22 (2017).
121. Grobe, A., Urai, J. L., Littke, R. & Lünsdorf, N. K. Hydrocarbon generation and migration under a large overthrust: The carbonate platform under the Semail Ophiolite, Jebel Akhdar, Oman. *Int. J. Coal Geol.* **168**, 3–19 (2016).
122. Mahanjane, E. S. *et al.* Maturity and petroleum systems modelling in the offshore zambezi delta depression and Angoche Basin, Northern Mozambique. *J. Pet. Geol.* **37**, 329–348 (2014).
123. Hakimi, M. H. & Abdullah, W. H. Modelling petroleum generation of Late Cretaceous Dabut Formation in the Jiza-Qamar Basin, Eastern Yemen. *Mar. Pet. Geol.* **61**, 1–13 (2015).
124. Ali, M. Y. & Lee, J. H. Petroleum Geology of the Nogal Basin and Surrounding Area, Northern Somalia, Part 2: Hydrocarbon Potential. *J. Pet. Geol.* **42**, 233–260 (2019).
125. Al-Areeq, N. M., Al-Badani, M. A., Salman, A. H. & Albaroot, M. A. Petroleum source rocks characterization and hydrocarbon generation of the Upper Jurassic succession in Jabal Ayban field, Sabatayn Basin, Yemen. *Egypt. J. Pet.* **27**, 835–851 (2018).
126. Svendsen, N. B. The Sahmah Formation of Oman: Exploration implications for the Rub' Al-Khali Basin. *GeoArabia* **9**, 119–136 (2004).
127. Makeen, Y. M. *et al.* Thermal maturity history and petroleum generation modelling for the Lower Cretaceous Abu Gabra Formation in the Fula Sub-basin, Muglad Basin, Sudan. *Mar. Pet. Geol.* **75**, 310–324 (2016).
128. Carminati, E. *et al. Tectonic Evolution of the Northern Oman Mountains, Part of the Strait of Hormuz Syntaxis: New Structural and Paleothermal Analyses and U-Pb Dating of Synkinematic Calcite*. *Tectonics* vol. 39 (2020).
129. Keshta, S., Metwalli, F. J. & Al Arabi, H. S. Analysis of petroleum system for exploration and risk reduction in Abu Madi/Elqar'a gas field, Nile Delta, Egypt. *Int. J. Geophys.* (2012) doi:10.1155/2012/187938.
130. Cole, G. A. Graptolite-Chitinozoan Reflectance and Its Relationship to Other Geochemical Maturity Indicators in the Silurian Qusaiba Shale, Saudi Arabia. *Energy and Fuels* **8**, 1443–1459 (1994).
131. Tiercelin, J.-J. *et al.* Hydrocarbon potential of the Meso-Cenozoic Turkana Depression, northern

Kenya. I. Reservoirs: depositional environments, diagenetic characteristics, and source rock–reservoir relationships. *Mar. Pet. Geol.* **21**, 41–62 (2004).
132. Abu-Ali, M. & Littke, R. Paleozoic petroleum systems of Saudi Arabia: A basin modeling approach. *GeoArabia* **10**, 131–168 (2005).
133. Cole, G. A. *et al.* Petroleum geochemistry of the Midyan and Jaizan basins of the Red Sea, Saudi Arabia. *Mar. Pet. Geol.* **12**, 597–614 (1995).
134. Wolela, A. Source Rock Potential of the Blue NIle (Abay) Basin, Ethiopia. *J. Pet. Geol.* **30**, 389–402 (2007).
135. Cole, G. A. *et al.* Organic Geochemistry of the Jurassic Petroleum System in Eastern Saudi Arabia. in *Pangea, global environments and resources: Canadian Society of Petroleum Geologists Memoir 17* 413–438 (1994).
136. El Nady, M. M. & Hakimi, M. H. The petroleum generation modeling of prospective affinities of Jurassic–Cretaceous source rocks in Tut oilfield, north Western Desert, Egypt: an integrated bulk pyrolysis and 1D-basin modeling. *Arab. J. Geosci.* **9**, (2016).
137. Morley, C. K. *et al.* Geology and Geophysics of the Anza Graben. in *Geoscience of Rift Systems-Evolution of East Africa: AAPG Studies in Geology No. 44* (ed. Morley, C. K.) 67–90 (1999).
138. Fleischer, R., Price, P. & Walker, R. *Nuclear Tracks in Solids: principles and applications*. (University of California Press, 1975).
139. Wagner, G. & Van den Haute, P. *Fission-Track Dating*. (Kluwer Academic Publishers, 1992).
140. Laslett, G. M., Green, P. F., Duddy, I. R. & Gleadow, A. J. W. Thermal annealing of fission tracks in apatite 2. A quantitative analysis. *Chem. Geol. Isot. Geosci. Sect.* **65**, 1–13 (1987).
141. Gleadow, A. J. W. & Duddy, I. R. A Natural Long-Term Track Annealing Experiment for Apatite. *Nucl. Tracks* **5**, 169–174 (1981).
142. Donelick, R. A., O'Sullivan, P. B. & Ketcham, R. A. Apatite Fission-Track Analysis. *Rev. Mineral. Geochemistry* **58**, 49–94 (2005).
143. Barbarand, J., Carter, A., Wood, I. & Hurford, T. Compositional and structural control of fission-track annealing in apatite. *Chem. Geol.* **198**, 107–137 (2003).
144. Coyle, D. A. & Wagner, G. A. Positioning the titanite fission-track partial annealing zone. *Chem. Geol.* **149**, 117–125 (1998).
145. Yamada, R., Tagami, T. & Nishimura, S. Confined fission-track length measurement of zirocn: assessment of factors affecting the paleotemperature estimate. *Chem. Geol. (Isotope Geosci. Sect.* **119**, 293–306 (1995).
146. Tagami, T. & Dumitru, T. A. Provenance and thermal history of the Franciscan accretionary complex: Constraints from zircon fission track thermochronology. *J. Geophys. Res. B Solid Earth* **101**, 11353–11364 (1996).
147. Rahn, M. K., Brandon, M. T., Batt, G. E. & Garver, J. I. A zero-damage model for fission-track annealing in zircon. *Am. Mineral.* **89**, 473–484 (2004).
148. Tagami, T., Galbraith, R. F., Yamada, R. & Laslett, G. M. Revised Annealing Kinetics of Fission Tracks in Zircon and Geological Implications. in *Advances in Fission-Track Geochronology* 99–112 (1998). doi:10.1007/978-94-015-9133-1_8.
149. Yamada, R., Murakami, M. & Tagami, T. Statistical modelling of annealing kinetics of fission tracks in zircon; Reassessment of laboratory experiments. *Chem. Geol.* **236**, 75–91 (2007).
150. Ketcham, R. A. Fission-Track Annealing: From Geologic Observations to Thermal History Modeling. in *Fission-Track Thermochronology and its Application to Geology* 49–75 (Springer International Publishing, 2019). doi:10.1007/978-3-319-89421-8_3.
151. Dunkl, I. Trackkey: a Windows program for calculation and graphical presentation of fission track data. *Comput. Geosci.* **28**, 3–12 (2002).
152. Galbraith, R. F. On statistical models for fission track counts. *Math. Geol.* **13**, 471–478 (1981).
153. Galbraith, R. F. & Laslett, G. M. Statistical models for mixed fission track ages. *Int. J. Radiat. Appl. Instrumentation. Part* **21**, 459–470 (1993).
154. Green, P. On the thermo-tectonic evolution of Northern England: evidence from fission track

analysis. *Geol. Mag.* **123**, 493–506 (1986).
155. Seiler, C., Boone, S. C., Kohn, B. P. & Gleadow, A. J. W. A grain-by-grain comparison of apatite fission-track analysis by LA-ICP-MS and the External Detector Method. *Chem. Geol.* **635**, 121623 (2023).
156. Gleadow, A. J. W. *et al.* Coincidence mapping – a key strategy for the automatic counting of fission tracks in natural minerals. *Geol. Soc. London Spec. Publ. Thermochronological Methods From Palaeotemperature Constraints to Landsc. Evol. Model.* **324**, 25–36 (2009).
157. Vermeesch, P. Statistics for LA-ICP-MS based fission track dating. *Chem. Geol.* (2017) doi:10.1016/j.chemgeo.2017.03.002.
158. Carlson, W. D., Donelick, R. A. & Ketcham, R. A. Variability of apatite fission-track annealing kinetics: II. Crystallographic orientation effects. *Am. Mineral.* **84**, 1224–1234 (1999).
159. Farley, K. A. Helium diffusion from apatite: General behavior as illustrated by Durango fluorapatite. *J. Geophys. Res.* **105**, 2903–2914 (2000).
160. Reiners, P. W. & Farley, K. A. Influence of crystal size on apatite (U-Th)/He thermochronology: An example from the Bighorn Mountains, Wyoming. *Earth Planet. Sci. Lett.* **188**, 413–420 (2001).
161. Shuster, D. L., Flowers, R. M. & Farley, K. A. The influence of natural radiation damage on helium diffusion kinetics in apatite. *Earth Planet. Sci. Lett.* **249**, 148–161 (2006).
162. Wildman, M. *et al.* The chronology and tectonic style of landscape evolution along the elevated Atlantic continental margin of South Africa resolved by joint apatite fission track and (U-Th-Sm)/He thermochronology. *Tectonics* **35**, 511–545 (2016).
163. Danišík, M. *et al.* Seeing is believing: Visualization of He distribution in zircon and implications for thermal history reconstruction on single crystals. *Sci. Adv.* **3**, 1–10 (2017).
164. Wolf, R. A., Farley, K. A. & Kass, D. M. Modeling of the temperature sensitivity of the apatite (U – Th)/He thermochronometer. *Chem. Geol.* **148**, 105–114 (1998).
165. Biswas, S. *et al.* Exhumation and uplift of the Shillong plateau and its influence on the eastern Himalayas: New constraints from apatite and zircon (U-Th-[Sm])/He and apatite fission track analyses. *Tectonics* **26**, (2007).
166. Reiners, P. W., Farley, K. A. & Hickes, H. J. He diffusion and (U-Th)/He thermochronometry of zircon: Initial results from Fish Canyon Tuff and Gold Butte. *Tectonophysics* **349**, 297–308 (2002).
167. Wolfe, M. R. & Stockli, D. F. Zircon (U-Th)/He thermochronometry in the KTB drill hole, Germany, and its implications for bulk He diffusion kinetics in zircon. *Earth Planet. Sci. Lett.* **295**, 69–82 (2010).
168. Stockli, D. F. & Farley, K. A. Empirical constraints on the titanite (U-Th)/He partial retention zone from the KTB drill hole. *Chem. Geol.* **207**, 223–236 (2004).
169. Gleadow, A., Harrison, M., Kohn, B., Lugo-zazueta, R. & Phillips, D. The Fish Canyon Tuff : A new look at an old low-temperature thermochronology standard. *Earth Planet. Sci. Lett.* **424**, 95–108 (2015).
170. Farley, K. A., Wolf, R. A. & Silver, L. T. The effects of long alpha-stopping distances on (U-Th)/He ages. *Geochim. Cosmochim. Acta* **60**, 4223–4229 (1996).
171. Brown, R. W. *et al.* Natural age dispersion arising from the analysis of broken crystals. Part I: Theoretical basis and implications for the apatite (U-Th)/He thermochronometer. *Geochim. Cosmochim. Acta* **122**, 478–497 (2013).
172. Gallagher, K. Evolving temperature histories from apatite fission-track data. *Earth Planet. Sci. Lett.* **136**, 421–435 (1995).
173. Nyblade, A. A. Terrestrial heat flow in east and southern Africa. *J. Geophys. Res. Solid Earth* **95**, 17371–17384 (1990).
174. Kohn, B. P., Eyal, M. & Feinstein, S. A major Late Devonian-Early Carboniferous (Hercynian) Thermotectonic event at the NW Margin of the Arabian-Nubian Shield: Evidence from zircon fission track dating. *Tectonics* **11**, 1018–1027 (1992).
175. Seward, D. An insight into the breakup of Gondwana : Identifying events through low-temperature thermochronology from the basement rocks of Madagascar. **23**, (2004).

176. Emmel, B., Jacobs, J., Kastowski, M. & Graser, G. Phanerozoic upper crustal tectono-thermal development of basement rocks from central Madagascar: An integrated fission-track and structural study. *Tectonophysics* **412**, 61–86 (2006).
177. Emmel, B., Jacobs, J. & Razakamanana, T. Titanite and apatite fission track analyses on basement rocks of central-southern Madagascar: Constraints on exhumation and denudation rates along the eastern rift shoulder of the Morondava basin. *J. African Earth Sci.* **38**, 343–361 (2004).
178. Bauer, F. U., Jacobs, J., Emmel, B. U. & van Soest, M. C. New (U-Th)/He titanite data from a complex orogen-passive margin system: A case study from northern Mozambique. *J. African Earth Sci.* **120**, 56–69 (2016).
179. Dietrich, P. *et al.* The Glacial Paleolandscapes of Southern Africa: the Legacy of the Late Paleozoic Ice Age. *EGUsphere* (2024).
180. Milani, E. J. & De Wit, M. J. Correlations between the classic Paraná and Cape-Karoo sequences of South America and southern Africa and their basin infills flanking the Gondwanides: Du Toit revisited. *Geol. Soc. Spec. Publ.* **294**, 319–342 (2008).
181. Merdith, A. S. *et al.* Extending full-plate tectonic models into deep time: Linking the Neoproterozoic and the Phanerozoic. *Earth-Science Rev.* **214**, 103477 (2021).
182. Merdith, A. S., Williams, S. E., Brune, S., Collins, A. S. & Müller, R. D. Rift and plate boundary evolution across two supercontinent cycles. *Glob. Planet. Change* **173**, 1–14 (2019).
183. Emmel, B., Geiger, M. & Jacobs, J. Detrital apatite fission-track ages in Middle Jurassic strata at the rifted margin of W Madagascar - Indicator for a protracted resedimentation history. *Sediment. Geol.* **186**, 27–38 (2006).
184. Jöns, N., Schenk, V., Appel, P. & Razakamanana, T. Two-stage metamorphic evolution of the Bemarivo Belt of northern Madagascar: Constraints from reaction textures and in situ monazite dating. *J. Metamorph. Geol.* **24**, 329–347 (2006).
185. Guiraud, R., Bosworth, W., Thierry, J. & Delplanque, A. Phanerozoic geological evolution of Northern and Central Africa: An overview. *J. African Earth Sci.* **43**, 83–143 (2005).
186. Delvaux, D., Maddaloni, F., Tesauro, M. & Braitenberg, C. The Congo Basin: Stratigraphy and subsurface structure defined by regional seismic reflection, refraction and well data. *Glob. Planet. Change* **198**, 103407 (2021).
187. Schull, T. J. Rift basins of interior Sudan: petroleum exploration and discovery. *Am. Assoc. Pet. Geol. Bull.* **72**, 1128–1142 (1988).
188. Ibrahim, A. E., Ebinger, C. J. & Fairhead, J. D. Interpretation of the Central African Rift system in Sudan based on new gravity and aeromagnetic data. *Eos (Washington. DC).* **462**, (1991).
189. Brune, S., Corti, G. & Ranalli, G. Controls of inherited lithospheric heterogeneity on rift linkage: Numerical and analog models of interaction between the Kenyan and Ethiopian rifts across the Turkana depression. *Tectonics* **36**, 1767–1786 (2017).
190. Wang, L., Maestrelli, D., Corti, G., Zou, Y. & Shen, C. Normal fault reactivation during multiphase extension: Analogue models and application to the Turkana depression, East Africa. *Tectonophysics* **811**, 228870 (2021).
191. Bosworth, W. & Morley, C. K. Structural and stratigraphic evolution of the Anza rift, Kenya. *Tectonophysics* **236**, 93–115 (1994).
192. Ruban, D. A., Al-Husseini, M. I. & Iwasaki, Y. Review of Middle East Paleozoic plate tectonics. *GeoArabia* **12**, 35–56 (2007).
193. Grobe, A. *et al.* Tectono-Thermal evolution of Oman's Mesozoic passive continental margin under the obducting Semail Ophiolite: A case study of Jebel Akhdar, Oman. *Solid Earth* **10**, 149–175 (2019).
194. Fox, M., Dai, J. G. & Carter, A. *Badly Behaved Detrital (U-Th)/He Ages: Problems With He Diffusion Models or Geological Models? Geochemistry, Geophysics, Geosystems* vol. 20 (2019).
195. Sousa, F. J. & Farley, K. A. A framework for evaluating variation in (U-Th)/He datasets. *Minerals* **10**, 1–15 (2020).
196. Tagami, T. & Shimada, C. Natural long-term annealing of the zircon fission track system around a

granitic pluton. *J. Geophys. Res. Solid Earth* **101**, 8245–8255 (1996).
197. Boone, S. C., Seiler, C., Reid, A. J., Kohn, B. & Gleadow, A. An Upper Cretaceous paleo-aquifer system in the Eromanga Basin of the central Gawler Craton, South Australia: evidence from apatite fission track thermochronology. *Aust. J. Earth Sci.* **63**, 315–331 (2016).
198. Seiler, C., Gleadow, A. J. W., Fletcher, J. M. & Kohn, B. P. Thermal evolution of a sheared continental margin: Insights from the Ballenas transform in Baja California, Mexico. *Earth Planet. Sci. Lett.* **285**, 61–74 (2009).
199. Reiners, P. W., Thomson, S. N., McPhillips, D., Donelick, R. A. & Roering, J. J. Wildfire thermochronology and the fate and transport of apatite in hillslope and fluvial environments. *J. Geophys. Res. Earth Surf.* **112**, (2007).
200. Gleadow, A. J. W., Duddy, I. R., Green, P. F. & Lovering, J. F. Confined fission track lengths in apatite: a diagnostic tool for thermal history analysis. *Contrib. to Mineral. Petrol.* **94**, 405–415 (1986).
201. Key, R. M., Cotterill, F. P. D. & Moore, A. E. The Zambezi River: An archive of tectonic events linked to the amalgamation and disruption of Gondwana and subsequent evolution of the African plate. *South African J. Geol.* **118**, 425–438 (2015).
202. Gernon, T. M. *et al.* Coevolution of craton margins and interiors during continental break-up. *Nature* **632**, 327–335 (2024).
203. McMillan, M., Gleadow, A., Kohn, B. & Seiler, C. Post Gondwana breakup evolution of the SE Australia rifted margin revisited. *Terra Nov.* **32**, 109–121 (2020).
204. van Hinsbergen, D. J. J. *et al.* A record of plume-induced plate rotation triggering subduction initiation. *Nat. Geosci.* **14**, 626–630 (2021).
205. Egan, S. S. The flexural isostatic response of the lithosphere to extensional tectonics. *Tectonophysics* **202**, 291–308 (1992).
206. Gunnell, Y., Gallagher, K., Carter, A., Widdowson, M. & Hurford, A. J. Denudation history of the continental margin of western peninsular India since the early Mesozoic - reconciling apatite fission-track data with geomorphology. *Earth Planet. Sci. Lett.* **215**, 187–201 (2003).
207. Gallagher, K., Hawkesworth, C. J. & Mantovani, M. S. M. The denudation history of the onshore continental margin of SE Brazil inferred from apatite fission track data. *J. Geophys. Res.* **99**, 18,117-18,145 (1994).
208. Murray, K. E., Braun, J. & Reiners, P. W. Toward Robust Interpretation of Low-Temperature Thermochronometers in Magmatic Terranes. *Geochemistry, Geophys. Geosystems* **19**, 3739–3763 (2018).
209. Pik, R. Geodynamics: East Africa on the rise. *Nat. Geosci.* **4**, 660–661 (2011).
210. McDowell, F. W., McIntosh, W. C. & Farley, K. A. A precise 40Ar-39Ar reference age for the Durango apatite (U-Th)/He and fission track dating standard. *Chem. Geol.* **214**, 249–263 (2005).